

Resistivity image beneath an area of active methane seeps in the west Svalbard continental slope

Bedanta K. Goswami,¹ Karen A. Weitemeyer,^{1,2} Timothy A. Minshull,¹
 Martin C. Sinha,¹ Graham K. Westbrook^{1,3,4} and Héctor Marín-Moreno²

¹*Ocean and Earth Science, University of Southampton, National Oceanography Centre Southampton, European Way, Southampton SO14 3ZH, United Kingdom. E-mail: bedanta.goswami@noc.soton.ac.uk*

²*National Oceanography Centre Southampton, European Way, Southampton SO14 3ZH, United Kingdom*

³*School of Geography, Earth and Environmental Sciences, University of Birmingham, Birmingham B15 2TT, United Kingdom*

⁴*Geosciences Marines, Ifremer Centre de Brest, F-29280 Plouzané, France*

Accepted 2016 September 1. Received 2016 August 2; in original form 2016 February 10

SUMMARY

The Arctic continental margin contains large amounts of methane in the form of methane hydrates. The west Svalbard continental slope is an area where active methane seeps have been reported near the landward limit of the hydrate stability zone. The presence of bottom simulating reflectors (BSRs) on seismic reflection data in water depths greater than 600 m suggests the presence of free gas beneath gas hydrates in the area. Resistivity obtained from marine controlled source electromagnetic (CSEM) data provides a useful complement to seismic methods for detecting shallow hydrate and gas as they are more resistive than surrounding water saturated sediments. We acquired two CSEM lines in the west Svalbard continental slope, extending from the edge of the continental shelf (250 m water depth) to water depths of around 800 m. High resistivities (5–12 Ωm) observed above the BSR support the presence of gas hydrate in water depths greater than 600 m. High resistivities (3–4 Ωm) at 390–600 m water depth also suggest possible hydrate occurrence within the gas hydrate stability zone (GHSZ) of the continental slope. In addition, high resistivities (4–8 Ωm) landward of the GHSZ are coincident with high-amplitude reflectors and low velocities reported in seismic data that indicate the likely presence of free gas. Pore space saturation estimates using a connectivity equation suggest 20–50 per cent hydrate within the lower slope sediments and less than 12 per cent within the upper slope sediments. A free gas zone beneath the GHSZ (10–20 per cent gas saturation) is connected to the high free gas saturated (10–45 per cent) area at the edge of the continental shelf, where most of the seeps are observed. This evidence supports the presence of lateral free gas migration beneath the GHSZ towards the continental shelf.

Key words: Electrical properties; Marine electromagnetics; Gas and hydrate systems; Arctic region.

1 INTRODUCTION

The Arctic continental margin contains large amounts of methane within hydrate bearing sediments (Kretschmer *et al.* 2015; Marín-Moreno *et al.* 2015b). Methane hydrates are ice-like solid substances that are stable under high pressure and low temperature conditions (Kvenvolden 1993). Due to the cold temperatures in the Arctic, hydrate can be stable at the seafloor in around 400 m water depths for bottom water temperatures close to 2 °C. Since the high latitudes are warming at a fast rate, these shallow marine hydrates are at risk of becoming unstable and dissociating (Biastoch *et al.* 2011; Hunter *et al.* 2013). Methane is an important greenhouse gas, so, if large quantities of methane are released from hydrate dissociation, it may

end up in the atmosphere and contribute to global warming (Archer 2007).

In 2008, numerous seafloor methane seeps were reported along the 400 m isobath in the West Svalbard continental margin (Westbrook *et al.* 2009), close to the landward edge of the gas hydrate stability zone (GHSZ). Concurrent observations of a 1 °C rise in ocean temperatures over the past three decades in the area (Westbrook *et al.* 2009) led to the suggestion of seeps originating from dissociating hydrate; a theory that is corroborated by numerical models (Reagan & Moridis 2009; Marín-Moreno *et al.* 2013; Thatcher *et al.* 2013). Subsequent scientific cruises to the area (Rajan *et al.* 2012; Berndt *et al.* 2014; Sahling *et al.* 2014) also reported methane seeps along the 400 m isobath and discovered a number of additional seeps in

shallower water depths where hydrate are not predicted to be stable. Some of these seeps were reported in water depths as shallow as 80–90 m (Sahling *et al.* 2014). While hydrate dissociation could be a plausible cause of the seeps around the 400 m isobath, it is unlikely to be the only factor. Westbrook *et al.* (2009) suggested up-slope migration of free gas beneath the GHSZ as another likely mechanism behind the seeps. Submersible dives have revealed colonies of methane consuming bacteria along with authigenic carbonate deposits around the 400 m isobath (Berndt *et al.* 2014). These deposits and recent geochemical analysis (Panieri *et al.* 2016) suggest the presence of long term methane seepage in the area. Hydrate dissociation in response to seasonal variation in bottom water temperatures (1–2 °C) was proposed as a cause for the long term seepage (Berndt *et al.* 2014). However, there are no pockmarks directly associated with the seep sites (Rajan *et al.* 2012; Sarkar *et al.* 2012; Sahling *et al.* 2014), as one might expect in areas of prolonged focused fluid flow (Hovland *et al.* 2002). The absence of pockmarks may be due to the coarse glacial sediments in the area. Subsurface lithological heterogeneity between marine and glaciogenic sediments is also thought to play an important role in the location and alignment of the observed seeps (Rajan *et al.* 2012; Sarkar *et al.* 2012).

Gas hydrate presence beneath the continental slope of Svalbard has been inferred on the basis of bottom simulating reflectors (BSRs) on seismic reflection data (Vogt *et al.* 1994; Westbrook *et al.* 2008; Hustoft *et al.* 2009; Rajan *et al.* 2012; Sarkar *et al.* 2012) and from seismic velocity anomalies (Westbrook *et al.* 2008; Chabert *et al.* 2011). This was later confirmed when gas hydrate was recovered from a shallow core at 890 m water depth (Fisher *et al.* 2011). Although the predicted landward edge of hydrate stability extends to around 390 m water depth, no simple BSR cutting across lithological reflectors has yet been identified in water depths shallower than 600 m (Chabert *et al.* 2011; Sarkar *et al.* 2012; Ker *et al.* 2014). A BSR is a seismic reflector that follows the seafloor but has opposite polarity. It is often caused by the phase change from solid hydrate to underlying free gas. The absence of a simple BSR could be due to increased heterogeneity where the glaciogenic sediments are more prevalent. They have a lower porosity and permeability and consequently, gas and hydrate are restricted to the more permeable marine sediment that are interbedded with the glaciogenic sediments (Chabert *et al.* 2011). It may also be caused by the frequency content of airgun data which results in the BSR reflection being masked by another seismic reflector (Sarkar *et al.* 2012). In addition, shallow free-gas signatures such as high amplitude reflectors and low-velocity anomalies are observed in the upper continental slope (Rajan *et al.* 2012; Sarkar *et al.* 2012) close to the methane seep sites. While seismic studies have shown evidence of shallow gas pockets around the predicted base of GHSZ (Sarkar *et al.* 2012), they have been unable to image any gas hydrate directly linked to the seeps. Since the methane seeps must be fed either by shallow dissociating hydrate or from a free gas reservoir beneath the seafloor, improved estimates of this methane inventory are crucial. Hydrate and gas saturation estimates also provide input to models predicting the future response of the subsurface methane to ocean temperature changes (Marin-Moreno *et al.* 2013, 2015a).

Controlled source electromagnetic (CSEM) data are sensitive to the bulk resistivity, which is affected by the presence of hydrate or/and free gas in the sediments. Hydrate and free gas are orders of magnitude more resistive than saline pore water and electrical resistivity logs are often used in drilling to detect them (Collett & Ladd 2000). The use of marine CSEM for hydrate detection was first suggested by Edwards (1997) and has been successful in various academic studies (e.g. Schwalenberg *et al.* 2005; Weitemeyer

et al. 2006a; Schwalenberg *et al.* 2010a,b; Weitemeyer & Constable 2010; Weitemeyer *et al.* 2011; Goswami *et al.* 2015; Attias *et al.* 2016). It was also used commercially in Japan for hydrate exploration (referenced within Constable *et al.* (2016)). In this paper, 2-D resistivity cross-sections obtained from inversion of CSEM data are presented for two lines acquired in the area of methane seeps, on the west Svalbard continental slope (Fig. 1). The resistivity models are then used to infer hydrate and free gas saturations for the two profiles.

2 REGIONAL SETTING

The CSEM study area (Fig. 1a) is located in the continental slope of the west Svalbard margin, in the inter fan region between the Isfjorden cross-shelf trough and the Kongsfjorden cross-shelf trough, to the west of Prins Karls Forland island. The stratigraphy of the area has been influenced by early Eocene seafloor spreading and subsequent sedimentation during periods of uplift, glacio-eustatic fluctuations and sediment transport by prevailing ocean currents (Eiken & Hinz 1993; Sarkar *et al.* 2011). The continental shelf and the upper continental slope has thick glaciogenic sediments that were deposited by Plio-Pleistocene glacial debris flows (Solheim *et al.* 1996; Sarkar *et al.* 2011). The distal slope contains thick contourite sediments (Eiken & Hinz 1993; Forsberg *et al.* 1999). On the basis of seismic velocity models, the thickness of the Cenozoic sediments in the study area varies from about 2 km near the continental shelf to about 4 km in the distal slope region (Ritzmann *et al.* 2004).

3 CSEM DATA ACQUISITION

The CSEM profiles were acquired using a CSEM transmitter—deep-towed active source instrument (DASI; Sinha *et al.* 1990), a deep-towed tri-axis electric-field receiver—Vulcan (Weitemeyer & Constable 2010; Constable *et al.* 2016) and 14 ocean-bottom electric-field (OBE) sensors (Minshull *et al.* 2005; Fig. 2). DASI has a 100 m long horizontal dipole antenna that was used to transmit a 1 Hz square wave current of approximately 81 A (zero to peak) during the survey. An altimeter and conductivity temperature depth (CTD) probe mounted on DASI records the tow height (~50 m) and tow depth of the transmitter during operation. The OBEs were put on the seafloor using a small remotely operated vehicle (ROV; Murton *et al.* 2012) dropping them from a height of approximately 2 m. The OBEs record the horizontal components of the electric field across their two orthogonal 12 m long dipole antennae, at a sampling rate of 125 Hz. The usable range of transmitter–receiver offsets is controlled by the noise floor ($10^{-13} \text{ V A}^{(-1)} \text{ m}^{-2}$) and saturation threshold ($10^{-9} \text{ V}^{(-1)} \text{ m}^{-2}$) of the pre-amplifiers used in the OBEs. Vulcan was towed at a constant offset of 350 m behind the centre of the DASI antenna using a 300 m tow rope attached to the back of the DASI antenna. The Vulcan data, with a short constant offset (350 m), has high sensitivity to the shallow sediments and it complements the OBE data, which are more sensitive to the deeper sediments, due to their relatively larger offsets. Vulcan records the vertical and cross-line electric fields across two orthogonal 1 m dipole antennae and the inline electric field across a 2 m dipole antenna at a 250 Hz sampling rate. A compass containing tiltmeters and pressure sensor mounted on Vulcan also records the heading, pitch, roll and depth of the instrument. Accurate positions for DASI and the ROV were obtained from an ultrashort base-line (USBL)

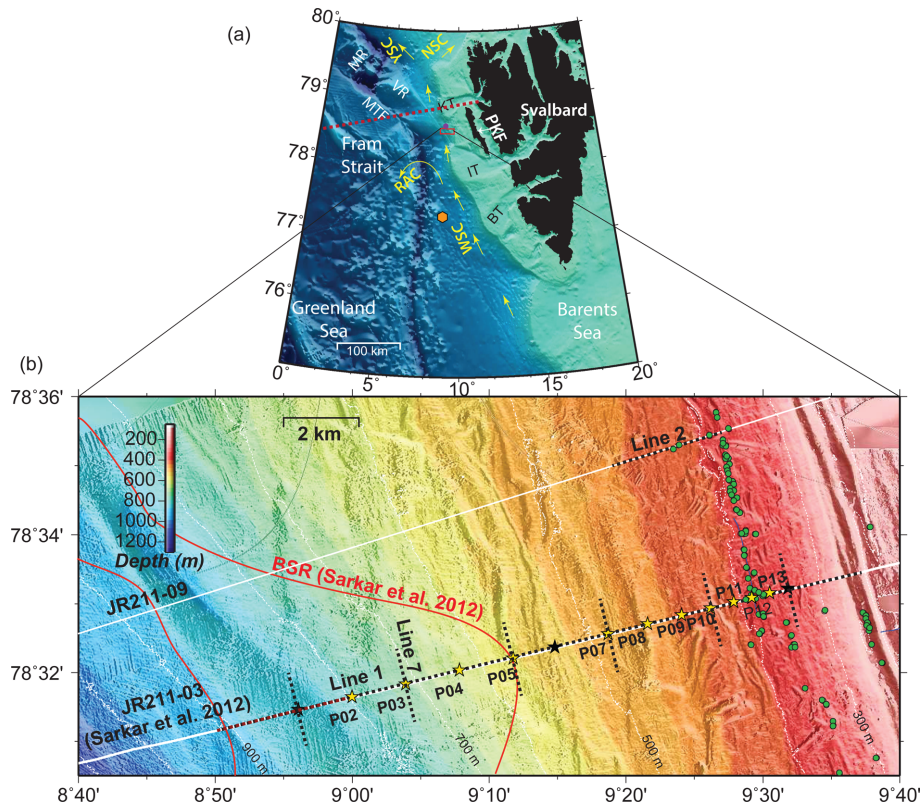


Figure 1. (a) Map of west Svalbard showing the continental slope survey area on the regional bathymetry map from international bathymetric chart of the Arctic Ocean (IBCAO) data (Jakobsson *et al.* 2008). The regional velocity models obtained from seismic refraction data shown by the dotted red line -AWI-994000 (Ritzmann *et al.* 2004) are used to infer basement depth for the study area. MR, Molloy Ridge; MTF, Molloy Transform Fault; VR, Vestnesa Ridge; PKF, Prins Karl Forland. Ocean currents—WSC, West Spitsbergen Current; NSC, North Spitsbergen Current; YSC, Yermak Slope Current; RAC, Return Atlantic Current—and cross-shelf troughs—KT, Kongsfjorden Trough; IS, Isfjorden Trough; BT, Bellsund Trough—affect the sedimentation. ODP Site 986 (orange polygon) provides reference resistivity and porosity. (b) Location of coincident CSEM (dotted black line) and seismic reflection survey lines (white lines) with multibeam bathymetry data. Green dots are the positions of the methane seeps observed in 2008. Ocean bottom electric-field (OBE) (yellow stars) records the CSEM data and the black stars show the OBEs that were not used for the CSEM inversion due to instrument errors. Initial 4.2 km (red dashed line) of Line 1 was discarded due to unknown DASI tow height.

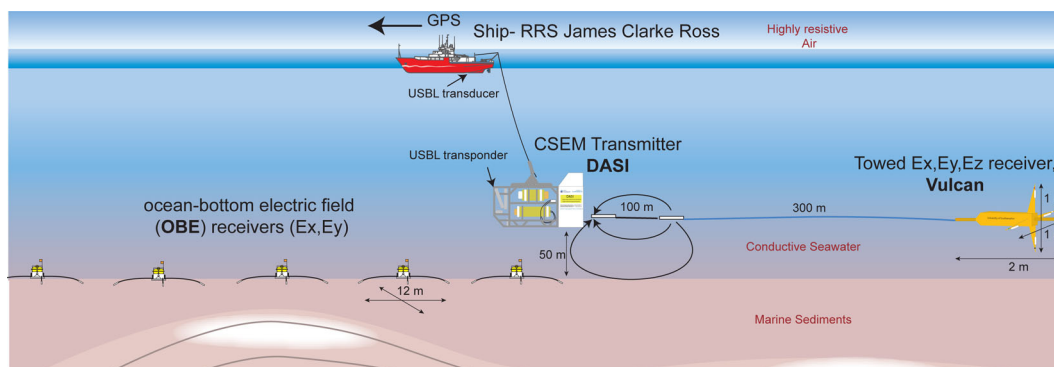


Figure 2. Sketch of the CSEM instrument layout used in the 2012 survey. CSEM transmitter, DASI, was towed 50 m above the seafloor and transmitted a 81 A current across its 100 m dipole. The Towed receiver, Vulcan (attached 300 m behind the DASI antenna), and the ocean bottom electric field receivers (OBEs), recorded the transmitted EM signal (reproduced from Goswami *et al.* 2015).

acoustic positioning system. The position of Vulcan was estimated during data analysis by assuming it followed the DASI track.

The CSEM survey was designed with the objective of obtaining a resistivity image beneath the region where the BSR is observed within the lower slope sediments (Sarkar *et al.* 2012) as well as the methane seeps around the 400 m isobath (Westbrook *et al.* 2009; Berndt *et al.* 2014; Sahling *et al.* 2014). Line 1 is approximately 18 km long, and was acquired in a roughly west to east direction. It

starts in the lower continental slope (around 900 m water depth) and finishes at the edge of the continental shelf (around 250 m water depth). The OBE spacing was decreased gradually from 1.5 km in the west to 250 m in the east, to cover the entire area of interest with the limited number of available instruments (14 OBEs). The OBE spacing was denser to the east as most of the features of interest were in shallower water depths. Line 2 was acquired to the north of Line 1 and is 3 km long extending from around 380 m water depth

to around 430 m water depth in a roughly east to west direction (Fig. 1b). Only Vulcan and DASI were used to acquire this line.

4 DATA ANALYSIS

4.1 CSEM data processing

The Earth's frequency domain transfer function (TF) can be extracted from the CSEM data, which are sensitive to changes in conductivity, source–receiver offset and other geometric factors (Constable 2010). The field data, which records the voltage difference across each receiver dipole were converted to the frequency domain using a fast Fourier transform over a 1-s window length. The amplitude and phase frequency response of the pre-amplifiers within each of the receivers were used to compute a calibrated voltage, which was then divided by the receiver dipole length to calculate the electric fields. The source response was then removed by normalizing the data with the source dipole moment (SDM) for each frequency to obtain the frequency domain Earth's TF. The current output by DASI was not reliably logged and only the voltage waveform was recorded for these CSEM lines. Based on analysis of other CSEM lines from the same survey that recorded the current accurately, an ideal waveform (1 Hz, 81 A) was used to compute the frequency domain SDMs. The voltage record was used to calibrate the start time of the ideal waveform to ensure phase accuracy in the frequency domain Earth's TF. Extremely noisy data outliers were manually removed and the 1 s data were then stacked to obtain a data point every 60 s, that has an improved signal-to-noise (S/N) ratio. This process provided data with an along-track sample interval of approximately 46 m.

Only the fundamental (1 Hz) and the first three harmonic frequencies (3, 5, 7 Hz) of OBE and Vulcan data were selected. Saturated OBE data and data below the noise floor were rejected. The OBEs saturate between 0 and 850 m offset and the maximum usable offset decreases from 2700 m at 1 Hz to 1700 m at 7 Hz. To reject air-wave contaminated data (Constable 2010), the maximum usable offset was reduced for the OBE sites shallower than 350 m water depth (P09 to P13) to 2100 m at 1 Hz, decreasing to 1500 m at 7 Hz. The first 4.2 km of Line 1 were discarded due to inaccuracies in the altitude reported by the DASI altimeter (Fig. 1b). This approach leaves us with no data from OBE P01 and very little data from OBE P02. In addition, data from OBEs P06 and P14 were discarded due to poorly matched electrodes. Based on S/N ratio analysis of the stacked data, all Vulcan data and most OBE data from transmissions between 1.8 and 3 km model distance on Line 1 were also rejected due to excessive noise of unknown origin.

The stacked OBE data were then rotated into the inline direction using the dipole orientations estimated by the orthogonal procrustes rotation analysis (OPRA) code (Key & Lockwood 2010). The angles obtained from OPRA were previously shown to have an accuracy of 3° (Key & Lockwood 2010). The amplitude and phase of inline OBE data were used as input into the OBE inversion. For the inversions of Vulcan data, the magnitude of the major axis of the polarization ellipse traced by the horizontal electric field vector (P_{\max}) (Smith & Ward 1974) was used. This approach was used because of uncertainties in Vulcan phase data, which might generate artefacts in the inversion model (Behrens 2005). The phase uncertainties arise due to ambiguities in transmitter and receiver orientations as well as unresolved timing issues between transmitter and the close offset Vulcan receiver.

4.1.1 Data uncertainty

The standard deviation computed in each stack provides a measure of noise in the data. While the cross-line component of Vulcan contained up to 10–15 per cent noise, the vertical component contained only about 1–2 per cent noise and the inline component about 0.05–0.1 per cent noise. In an ideal scenario, the recorded inline component of the electric field is along the transmitter dipole and $P_{\max} = E_{\text{inline}}$. In this study, the contribution of the recorded inline component to P_{\max} was greater than 98 per cent. A 1 per cent data error was specified for the inversion to account for navigational uncertainty.

The standard deviation of the OBE data suggest less than 1.5 per cent noise in the inline component for the data range selected for the inversion. A composite model uncertainty analysis following Myer *et al.* (2011) suggests a maximum total uncertainty (location uncertainty, antenna dips and noise) of 2.5 per cent for the OBE data. Based on forward model perturbations, an additional 0.5 per cent error was assigned to account for inaccuracies in the phase of the data as a result of using an ideal waveform during processing rather than a recorded waveform. A 3 per cent error was therefore assigned for the OBE inversion.

4.2 CSEM inversion

The MARE2DEM code (Key & Ovall 2011) was used to invert the CSEM data from the OBEs and Vulcan. OBE and the Vulcan data were inverted separately to obtain independent resistivity models. MARE2DEM uses a 2.5D finite element forward code (Key & Ovall 2011) and a fast implementation of Occam's inversion (Constable *et al.* 1987) to obtain the smoothest resistivity model from the family of models that can fit the data. It does so by automatically optimizing the values of Lagrange's multiplier and model roughness (Constable *et al.* 1987; Key 2012) for the specified misfit tolerance and data error.

A simple starting model was specified containing a highly resistive air layer ($10^{12} \Omega\text{m}$), seawater with three horizontal layers of constant resistivity (Fig. 3) and a starting resistivity of 1 Ωm for the sediments beneath the seafloor. Synthetic model studies suggest a notable effect of seawater resistivity on the inverted resistivity of shallow sediments. However, it was not possible to specify more details for the deepest water layer because of minimum angle restrictions on triangular elements in MARE2DEM ($\sim 30^\circ$) (Key & Ovall 2011). Specifying more detail in the bottom water layer led to minimum angle criteria being violated at the intersections of water layer boundaries and the dipping seafloor. Nevertheless, tests with a range of seawater resistivity values between 0.3 and 0.35 Ωm for the bottom layer showed that the effect of this parameter on the final OBE model was negligible. Vulcan inversions were found to be more sensitive to the seawater resistivity profile, but tests showed the chosen resistivity profile was also suitable for the Vulcan inversion. A seafloor bathymetry determined by summing the depth recorded by the CTD and altitude recorded by altimeter was specified. The air and seawater resistivity were fixed and the inversion was used to solve for the sediment resistivity. An inversion mesh of triangular elements that is finer beneath the seabed and coarser beyond the profile edges and with depth was used. The minimum edge length of the triangular elements was 50 m for the OBE inversion (26 830 free parameters). Elements with smaller edge lengths led to significant extra burden on the compute times due to the large number of additional free inversion parameters. The minimum edge length was 30 m for the Vulcan inversion, in which a finer mesh for the top

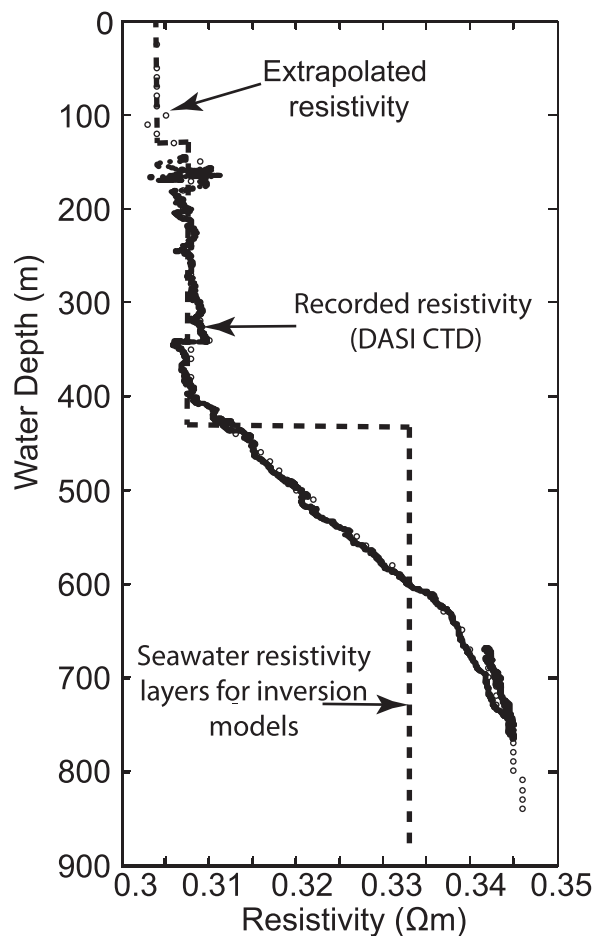


Figure 3. Resistivity of the water column obtained from the CTD mounted on DASI frame during its operation on Line 1. There is no information from the CTD above 150 m as the CTD was switched off at 150 m beneath the sea-surface.

600 mbsf (versus approximately 2 km for OBE inversion) was specified. Edge lengths less than 30 m are not allowed for the seafloor profile due to minimum angle restrictions ($\sim 30^\circ$). The regularized Occam inversion (Constable *et al.* 1987) requires specification of a target misfit to produce an appropriate model. Initially, the Occam inversion was specified a low target misfit (e.g. 0 or 0.1), which is never achieved. An appropriate target misfit was then estimated by analysing the variation of misfit with Lagrange's multiplier in this initial inversion. The lowest root-mean-square (RMS) misfit achieved in the initial inversion was chosen as the target misfit and the inversion was re-run with the new target value (Table 1).

2-D resistivity models inverted from inline CSEM data are sensitive to horizontal as well as vertical resistivity (Constable 2010; Ramananjaona *et al.* 2011; MacGregor & Tomlinson 2014). Both isotropic and vertical transverse isotropic (VTI) ($\rho_x = \rho_y \neq \rho_z$)

inversions were therefore run for the CSEM lines with a horizontal to vertical smoothing ratio of 3:1. Anisotropic penalty was 1 for the VTI inversions. The two inversions resulted in very similar resistivity models for the chosen target misfits. However, the horizontal resistivity models obtained from the VTI inversion are unlikely to be suitable for detailed analysis as no cross-line data were used (Ramananjaona *et al.* 2011). Nevertheless, in the presence of anisotropy, the smooth vertical resistivity models obtained from VTI inversions are expected to be more accurate than those obtained from an isotropic inversion (Ramananjaona *et al.* 2011; MacGregor & Tomlinson 2014; Myer *et al.* 2015), and in the absence of anisotropy, identical to the results of an isotropic inversion (Myer *et al.* 2015). Therefore, the focus of the discussions is on the smooth vertical resistivity models from the VTI inversions. The isotropic inversion models are also shown in the supplementary figures (Supporting Information Figs S1 and S2) to demonstrate similarity to the vertical resistivity models.

5 RESISTIVITY MODELS

5.1 Line 1 Vulcan inversion

The vertical resistivity model obtained from VTI inversion of Vulcan data shows significant lateral resistivity variation in the shallow subsurface (Fig. 4a). A good fit between data and model (Fig. 4b) is observed for Line 1. Synthetic data generated for a dipping antenna were inverted using the known as well as no dip information. Observation of residuals of these synthetic tests suggests lack of DASI antenna dip information is a likely cause of the small frequency dependent bias on the normalized residuals (Fig. 4c). A zone of 4–12 Ωm resistivity is observed within the lower slope sediments (700–800 m water depth) between 0 and 2 km model distance. Similar high resistivity is also observed on the resistivity model of a crossing-line at the western edge of Line 1 (Supporting Information Fig. S3). A resistivity of 3–4 Ωm is then observed from 4 to 10.5 km model distance within the upper slope sediments (approximately 675–380 m water depth) (Fig. 4a). The resistivity increases eastwards reaching 5–8 Ωm , with pockets of around 10 Ωm , within the upper continental slope sediments between 11 and 14 km model distance (water depths of around 210–380 m). The resistivity decreases with depth to the starting model resistivity of 1 Ωm , throughout the profile.

5.2 Line 1 OBE inversion

The vertical resistivity model obtained from VTI inversion of the OBE data (Fig. 5) shows 3–4 Ωm resistivity within the top 200 mbsf between 0 and 8 km model distance. A good fit between data and model (Fig. 6) is also observed for the OBE inversions. A thin resistive feature with 4–6 Ωm resistivity is observed approximately 100 mbsf at 8 km model distance which becomes gradually shallower landward, eventually reaching the seafloor around 12.5 km

Table 1. Detail of OBE and Vulcan inversions for the resistivity models shown for Line 1 and Line 2.

Line name	Inversion type	Receiver type	Data type	Target misfit	Iterations
Line 1	Isotropic	OBE	Log amplitude, phase	1	13
Line 1	VTI	OBE	Log amplitude, phase	0.88	9
Line 1	Isotropic	Vulcan	P_{max}	1	13
Line 1	VTI	Vulcan	P_{max}	1	11
Line 2	Isotropic	Vulcan	P_{max}	1	10
Line 2	VTI	Vulcan	P_{max}	1	9

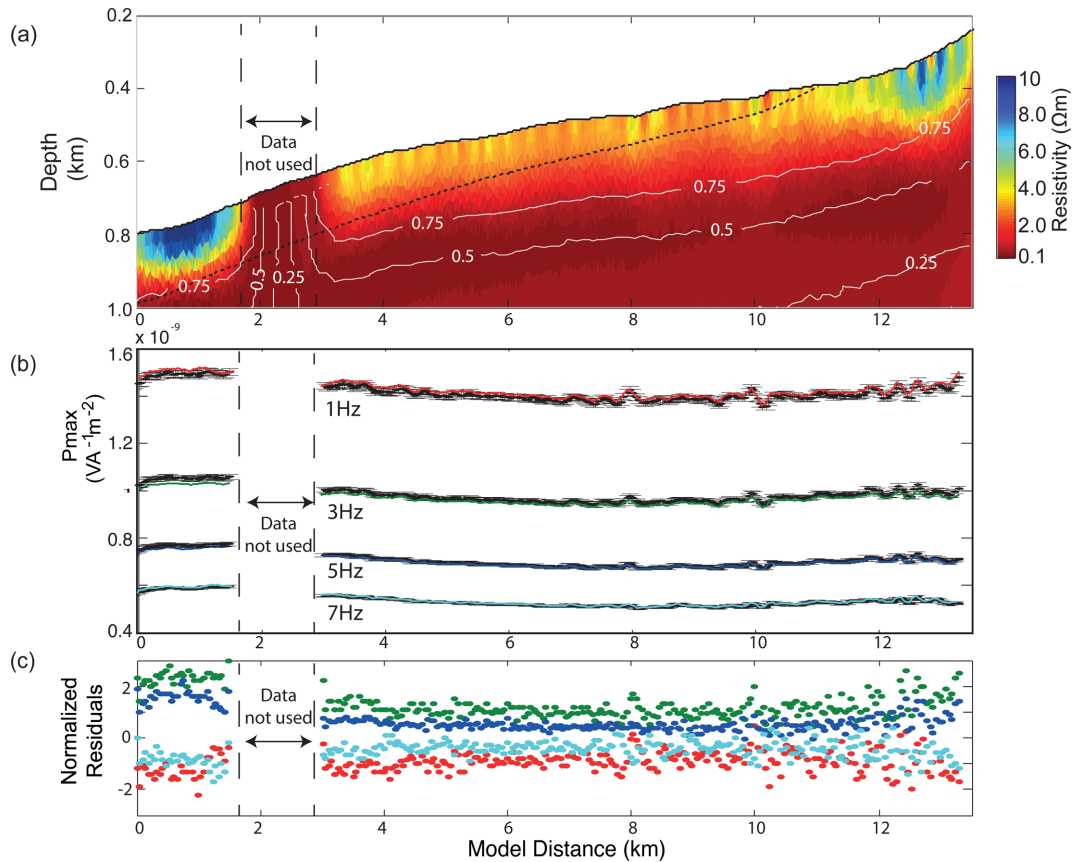


Figure 4. (a) Vertical resistivity model obtained from VTI inversion of Vulcan P_{\max} data for Line 1 showing significant lateral variation in resistivity. The predicted base of GHSZ from Marin-Moreno *et al.* (2013) is shown as a dashed line. Noisy data between 1.8 and 3 km model distance were not included in the inversion. Contour overlay (thin white line) shows data sensitivity to model features (0.5 = 50 per cent sensitivity). (b) Data (dots) and model (solid lines: 1 Hz–red, 3 Hz–green, 5 Hz–blue, 7 Hz–cyan) shows a good fit of the anisotropic model. (c) The residuals (1 Hz–red, 3 Hz–green, 5 Hz–blue, 7 Hz–cyan) normalized by their respective data error are collectively scattered around 0. However, a slight bias can be observed at each individual frequency likely related to the unknown dip of DASI antenna.

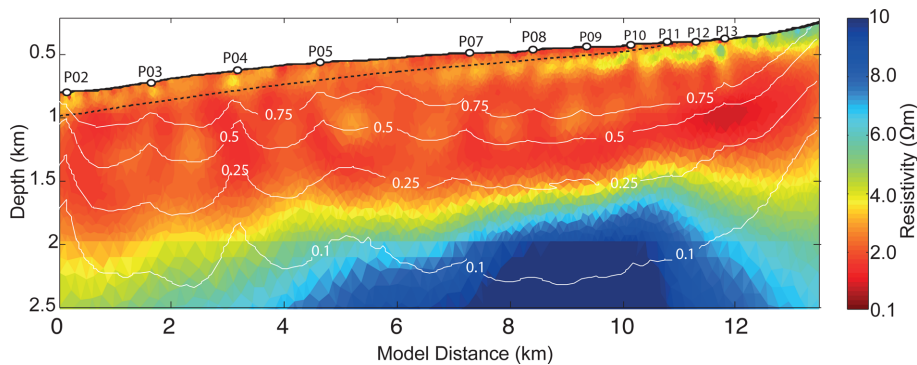


Figure 5. Vertical resistivity model for Line 1 obtained from VTI inversion of OBE amplitude and phase data. The predicted base of GHSZ from Marin-Moreno *et al.* (2013) is shown as a dashed line. Contour overlay (thin white line) shows data sensitivity to model features (0.5 = 50 per cent sensitivity).

model distance. Resistivities of 1.5–2 Ωm are observed between 200 mbsf and 1000 mbsf with few regions containing values of 3–4 Ωm. Beneath 1000 mbsf, the resistivity gradually increases to around 12–15 Ωm.

5.3 Line 2

The vertical resistivity model (Fig. 7a) obtained from VTI inversion of Vulcan P_{\max} data for Line 2 shows a steady increase in resistivity from west to east within the shallow subsurface sediments. The

resistivity of 3–4 Ωm beneath water depths of 410 m (1.5 km model distance) to 430 m (3 km model distance) gradually increases to 5–8 Ωm resistivity for water depths shallower than 410 m (0–1.5 km model distance). A good fit between data and model predictions (Fig. 7b) is observed for Line 2.

6 DISCUSSION

Two sets of EM receivers (Vulcan and OBEs) were used in this survey with an aim to resolve both shallow and deep subsurface

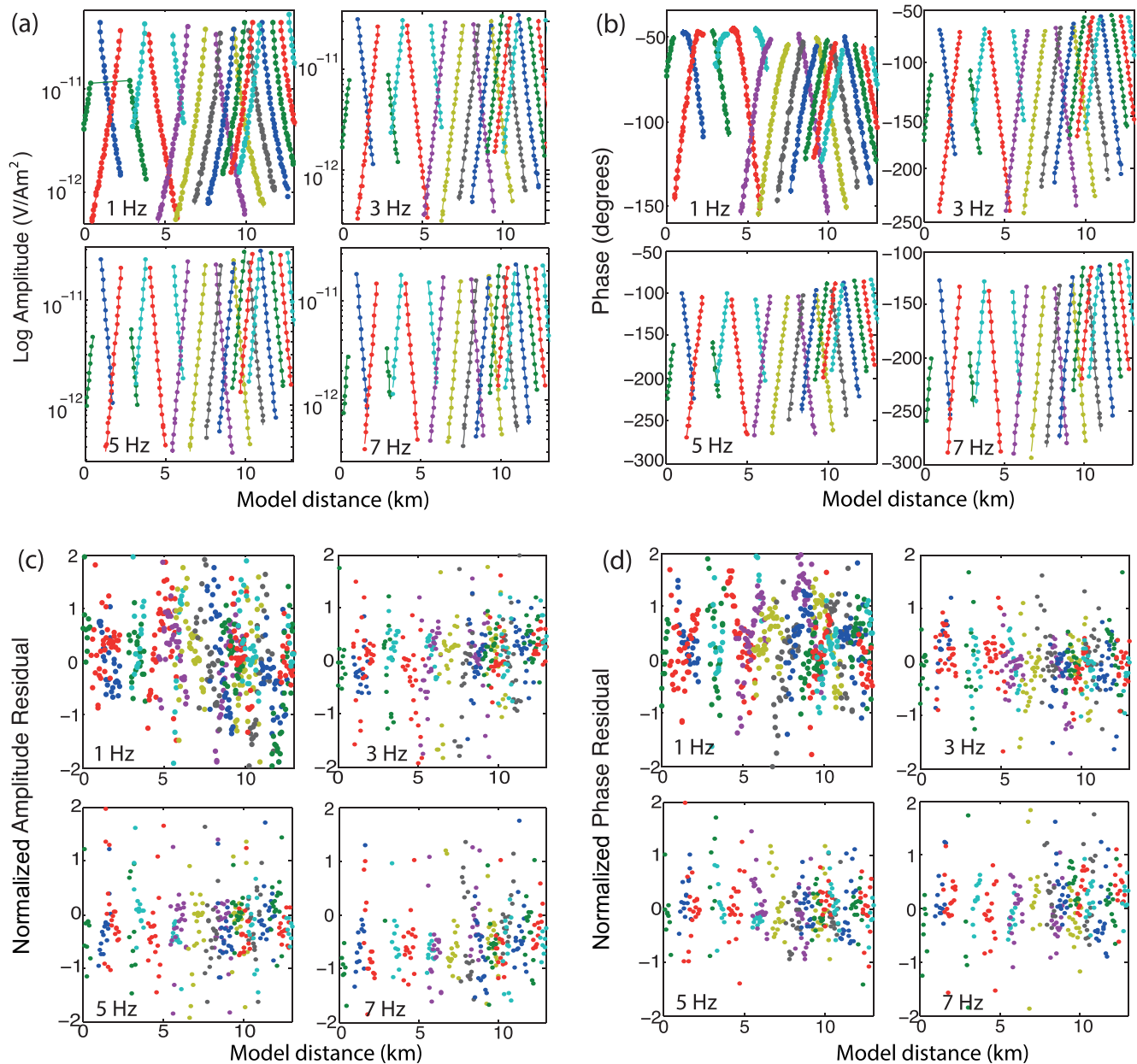


Figure 6. This figure shows the model (solid lines) fit to OBE data (solid circles) for 1, 3, 5, 7 Hz frequencies used in the inversion. (a) Amplitude (error bars are too small in the log scale display to be visible), (b) phase, (c) normalized amplitude residuals and (d) normalized phase residuals show a good model to data fit for the target misfit of 0.88 and 3 per cent data uncertainty. The residuals are normalized by their respective data error. A gradual increase in amplitude and phase towards the end of the line is also observed in the data as seen by the higher resistivity in the resistivity models shown in Fig. 5.

resistivity features. Although the Occam inversion outputs the smoothest model, it is also possible to fit more complicated models to the data for the given error. Unlike a Bayesian inversion (Chen *et al.* 2007; Buland & Kolbørnsen 2012; Ray & Key 2012), it does not provide any information about model uncertainty. Finding the suite of these models would require the application of many perturbations to the final model, that is impractical, given model run times (On 64 computer nodes 4x Xeon E5/Core i7 processors, the OBE inversions take approximately 20 hr and the Vulcan inversions take approximately 14 hr for Line 1 and 8 hr for Line 2). Another important consideration while interpreting the models is to determine whether any of the features seen are inversion artefacts. The resistivity models obtained from the inline CSEM data are primarily sensitive to transverse resistance (Constable 2010) (the product

of resistivity and thickness). When we consider the nature of the inversion approach, the variation in the size of the inversion grids with depth, and the trade-off between resistivity and thickness to recover the transverse resistance, it is difficult to quantify the resolution of the models. It would also require careful consideration of the dependence on frequency, available data range, noise and data errors in any such analysis (Constable 2010). Synthetic model inversions can provide qualitative but useful information about sensitivity and resolution (Goswami *et al.* 2015; Myer *et al.* 2015), and we take this approach here. The synthetic models generated using the frequencies of interest (1, 3, 5 and 7 Hz) are used to estimate the maximum depth sensitivity of Vulcan and sensitivity of the CSEM experiment to shallow and deep features observed in the resistivity models.

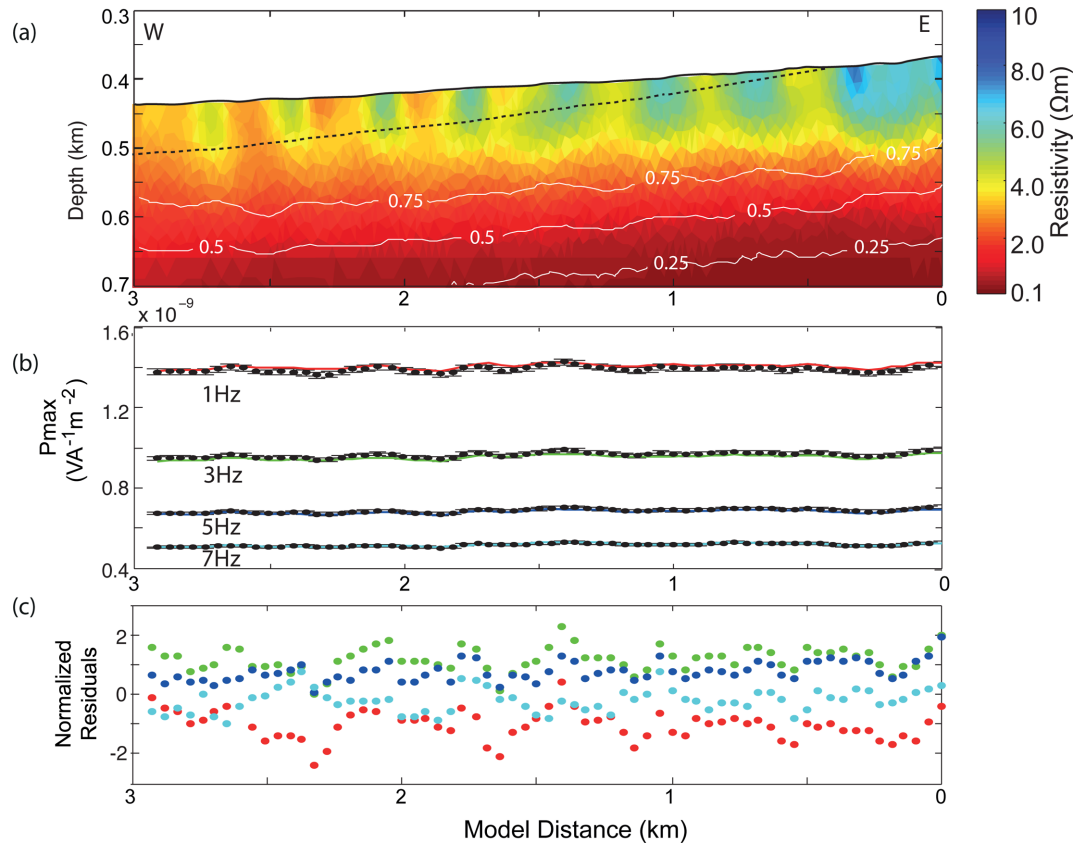


Figure 7. (a) Vertical resistivity model obtained from VTI inversion of Vulcan P_{max} data for Line 2. The predicted base of GHSZ obtained using estimates of Marin-Moreno *et al.* (2013) is shown as a dashed line. Contour overlay (thin white line) shows data sensitivity to model features (0.5 = 50 per cent sensitivity). (b) Data (dots) with error bars and model fit (solid lines: 1 Hz–red, 3 Hz–green, 5 Hz–blue, 7 Hz–cyan). (c) The residuals (1 Hz–red, 3 Hz–green, 5 Hz–blue, 7 Hz–cyan) normalized by their respective data error are collectively scattered around 0. However, a slight bias can be observed at each individual frequency likely related to the unknown dip of the DASI antenna.

6.1 Vulcan depth sensitivity

The Vulcan P_{max} data are computed for a single, short (350 m) source–receiver offset. Therefore, the data overlap for the Vulcan inversion is proportional to the number of frequencies used. The Vulcan inversion models are only expected to be sensitive to the very shallow sediments (150–250 m). The sensitivity matrix obtained from the Jacobian of the Occam inversion (Constable *et al.* 1987) provides information about the data’s sensitivity to model parameters. These suggest 50 per cent sensitivity to model parameters around 400 mbsf (e.g. Figs 4a and 7a). We used 2-D synthetic models and inversions to further understand the depth sensitivity of the Vulcan P_{max} data. For the synthetic tests, DASI and Vulcan are assumed to maintain a constant altitude of 50 m above a flat seafloor at 750 m water depth, with a separation of 350 m. The Earth is assumed to be isotropic, consisting of an insulating air layer ($10^{12} \Omega\text{m}$), conducting seawater of $0.3 \Omega\text{m}$ and resistive sediments. In the first scenario, a $3 \Omega\text{m}$ overburden of varying thickness is assumed to terminate at a $0.3 \Omega\text{m}$ conductive half-space (Fig. 8a). A $0.3 \Omega\text{m}$ resistivity is chosen for the terminating conductor to help with interpretation as it is significantly lower than starting model resistivity of $1 \Omega\text{m}$. Vulcan inversion models result in a terminating conductor that fall back to the starting half-space of $1 \Omega\text{m}$ (e.g. Fig. 7). For the second scenario, a $1 \Omega\text{m}$ overburden resistor of varying thickness and a $5 \Omega\text{m}$ terminating resistor was assumed (Fig. 8b). The thickness of the overburden layer is varied from 100 m to 350 m (Figs 8a and b). Random Gaussian noise was

added to the synthetic data that is similar to the noise in the real data (0.1 per cent of datum) for both model scenarios. A starting model consisting of fixed air and water layers from the true model and starting sediment resistivity of $1 \Omega\text{m}$ was specified. The minimum edge length of the triangular mesh is set to be 30 m for the top 1000 mbsf, increasing in size with depth and towards the ends of the synthetic profile. The inversions of both synthetic models converged to the target misfit of 1 within 10 iterations producing a good model fit to data.

Since inline CSEM data is mainly sensitive to the transverse resistance (resistivity \times layer thickness) for the chosen water depths (Constable 2010; MacGregor & Tomlinson 2014) and the Occam inversion outputs a smooth model, a combination of transverse resistance and resistivity is the preferred way to qualify sensitivity to a subsurface feature. Based on observations of various synthetic tests, the inverted transverse resistance of the overburden layer recovered to within 15 per cent of true value is considered a criterion for sensitivity. The inverted resistivity of the terminating layer recovered to within ~ 33 per cent of true resistivity is considered as another criterion for sensitivity. The resistivity tolerance is much higher than the transverse resistance threshold because it is easier to identify $0.1 \Omega\text{m}$ resistivity differences in the inversion results, which is ~ 33 per cent for the $0.3 \Omega\text{m}$ terminating conductor. For both the terminating conductor (Fig. 8a, Table 2) and terminating resistor (Fig. 8b, Table 3) tests, the joint transverse resistance and resistivity tolerances are satisfied by the models up to 250 m overburden thickness. There is an arguable sensitivity for the 300 m

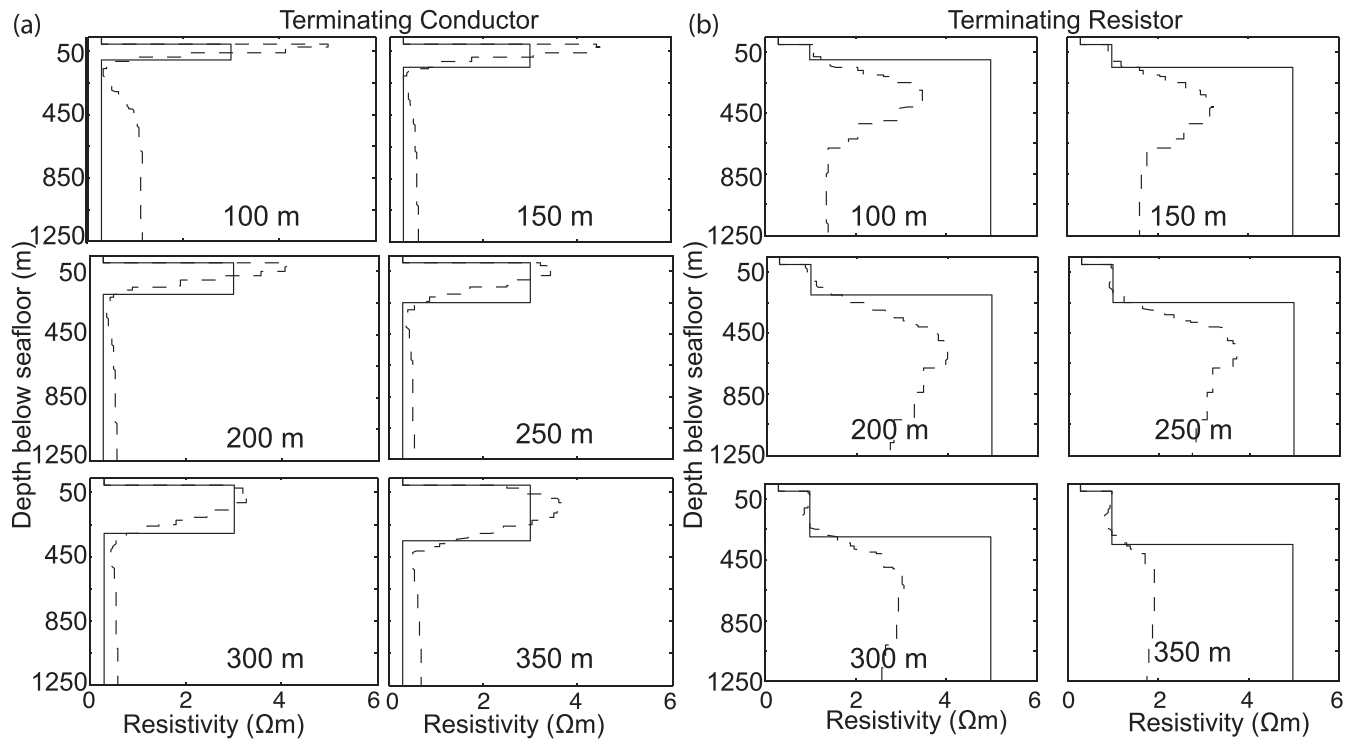


Figure 8. (a) Synthetic models showing different depths to the terminating 0.3 Ωm conductor beneath a 3 Ωm resistor. (b) Synthetic models showing different depths to the terminating 5 Ωm resistor beneath a 1 Ωm resistor. The true models are shown by the solid lines and the 2-D inversion results are shown by the dashed lines. The test suggests 250 m depth sensitivity for Vulcan.

Table 2. Transverse resistance calculations for the synthetic model and inverted models shown in Fig. 8(a). The transverse resistances are estimated using a resistivity of 3 Ωm and thickness interval beneath the seafloor shown in column 1.

Thickness (m)	True (Ωm^2)	Recovered (Ωm^2)	Conductor depth (m)
100	300	317	150
150	450	410	180
200	600	520	250
250	750	542	310
300	900	751	<0.4 Ωm not recovered
350	1050	1010	<0.4 Ωm not recovered

Table 3. Transverse resistance calculations for the synthetic model and inverted models shown in Fig. 8(b). The transverse resistances are estimated using a resistivity of 1 Ωm and thickness interval beneath the seafloor shown in column 1.

Thickness (m)	True (Ωm^2)	Recovered (Ωm^2)	Resistor depth (m)
100	100	112	240
150	150	151	250
200	200	217	250
250	250	305	300
300	300	298	>3.3 Ωm not recovered
350	350	343	>3.3 Ωm not recovered

model, but we suggest a conservative estimate of 250 m for Vulcan depth sensitivity based on this analysis. The synthetic tests along with the Jacobian sensitivity overlays suggest the high resistivity zones in the Vulcan inversion models (Figs 4 a and 7a) are therefore likely to be real features.

6.2 Shallow resistivity

Shallow resistive features can be observed in all of the resistivity models. The Vulcan depth sensitivity tests (Fig. 8) suggest that the shallow resistive zones observed in the Vulcan models are real. The Vulcan models (Fig. 4) are expected to better resolve the shallow resistivity between 0 and 8 km model distance than the OBE models (Fig. 5) due to the relatively large minimum usable offset (850 m) and large spacing between OBEs. However, the models differ more between 0 and 2 km model distance (Figs 4 and 5) than elsewhere. This difference arises because only long range (large transmitter–receiver offset) OBE data are available between 0 and 3 km model distance due to issues with transmitter altitude and noise (discussed in Section 4.1). This issue causes poor resolution of the shallow resistivity in the OBE models in this area.

Synthetic models with an ideal survey geometry are used to compare sensitivity to shallow resistors in OBE and Vulcan inversions. An insulating air layer (10^{12} Ωm), 0.3 Ωm seawater resistivity, a flat seafloor at 750 m water depth with sediment half-space resistivity of 3 Ωm is assumed. A 2.2 km long and 100 m thick resistor is designed to be buried 50 mbsf, between 1 and 3.2 km model distance (Fig. 9a). The synthetic Vulcan P_{max} data are generated for DASI and Vulcan at 50 m above the seafloor. Synthetic amplitude and phase OBE data are generated for OBEs placed at 1, 2.5, 4 and 7 km model distance to simulate the large spacing between OBEs in the deep waters. Random noise with a Gaussian distribution that is 0.1 per cent and 2 per cent of datum was added to Vulcan and OBE synthetic data respectively. The same starting model and inversion mesh is used as the Vulcan sensitivity tests. Both OBE and Vulcan synthetic model inversions converged in five iterations to the target misfit of 1 with a good model fit to data. The synthetic inversions show that the Vulcan model (Fig. 9b) is better at recovering the shape and lateral extent of the shallow resistor compared to the

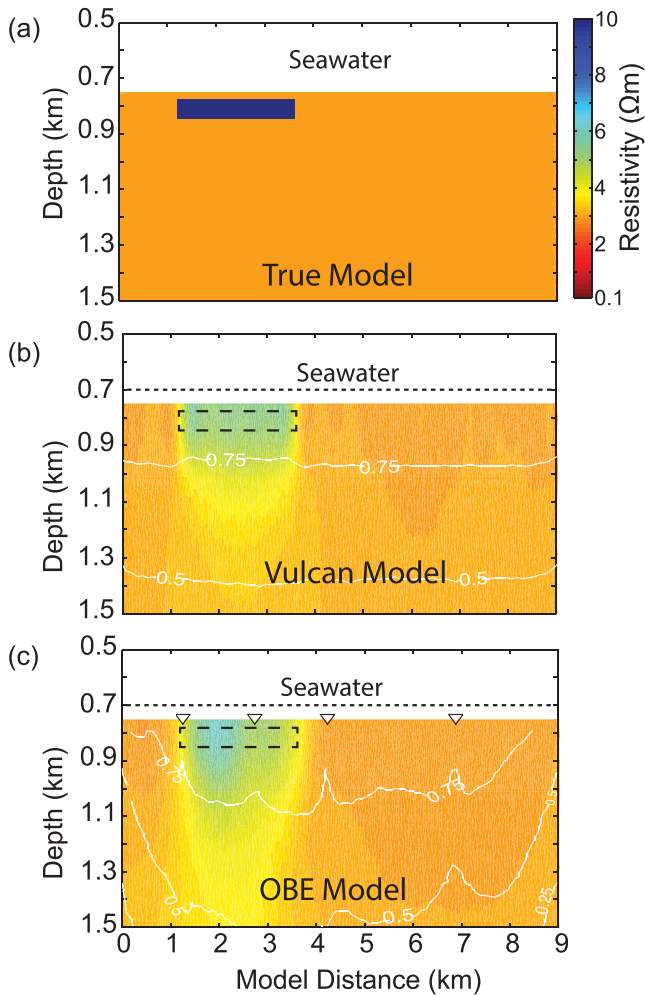


Figure 9. Synthetic models showing sensitivity of OBE and Vulcan data to shallow resistors. (a) The synthetic model contains a 2.2 km long, 100 m thick $10 \Omega\text{m}$ resistor buried 50 m beneath the seafloor. (b) P_{max} inversion of synthetic Vulcan data. DASI and Vulcan are shown by the dashed line. (c) Amplitude and phase inversion of synthetic OBE data for OBE locations shown by triangles and DASI height shown by the dashed line. Sensitivity of data to model are shown by the sensitivity contours (white lines: e.g. 0.5 = 50 per cent sensitivity) in panels (b) and (c). Data between 0 and 850 m transmitter–receiver offset for OBE data were not used in these synthetic inversions in order to simulate the real data available for inversion. The Vulcan model recovers the buried resistor slightly better than the OBE model. However, both OBE and Vulcan models underestimate the resistivity of the $10 \Omega\text{m}$ resistor.

OBE model (Fig. 9c). Vulcan also appeared to be able to provide a better limit on the depth of the lower boundary of the resistor. However, both inversions recovered similar resistivity (6–8 Ωm instead of $10 \Omega\text{m}$ true resistivity) for the shallow resistor. The inversions of both the OBE and Vulcan data are therefore expected to be sensitive to shallow resistive features. The inversion of the Vulcan data provide a more accurate representation of the shallow features due to the short offset data collected with Vulcan and the saturation limits of the OBE data (0–850 m offsets).

6.3 Gas hydrate and free gas

The models show both vertical and lateral variation in subsurface resistivity. The bulk resistivity of sediments depends on various

factors such as porosity, pore fluid saturation, pore fluid salinity, temperature, mineralogy and grain fabric of the host sediments (Ellis *et al.* 2010) which are poorly known for the study area. Coincident seismic reflection data sets JR211-03 (for Line 1) and JR211-09 (for Line 2) (Sarkar *et al.* 2012), however, provide some constraints to help with the interpretation of the shallow (0–400 mbsf) sub-surface sediments.

6.3.1 Interpretation of resistivity models

The thickness of the predicted GHSZ obtained from the non-steady state hydrate stability models of Marin-Moreno *et al.* (2013) varies from approximately 200 m at 800 m water depth to 0 m at around 390 m water depth. The models from the Vulcan inversions are therefore used for the interpretation of the GHSZ, as they are likely to be more sensitive to the top 250 mbsf. A BSR on JR211-03 (Sarkar *et al.* 2012) beneath the 4–12 Ωm resistivity between 0 and 2 km model distance on Line 1 suggests that the high resistivity zone may be caused by the presence of hydrate in water depths greater than 700 m (Fig. 10). The region of 3–4 Ωm resistivity within the GHSZ, between 4 and 10.5 km model distance on Line 1 (Fig. 10) and 1–3 km model distance on Line 2 (Fig. 11) does not contain any seismic signatures that indicate hydrate on the seismic reflection data. However, Chabert *et al.* (2011) suggest some hydrate in these water depths on the basis of high velocity anomalies. The resistivity of these shallow sediments are higher than the resistivity of hemipelagic sediments recorded at ODP Site 986 (Jansen *et al.* 1996; Fig. 12a), where no direct evidence of hydrate presence was documented. Although ODP Site 986 is located in 2036 m water depth and approximately 300 km to the south west of the study area (Fig. 1), it is the only available nearby resistivity log. If we assume that there are no significant differences in porosity and sediment composition between the study area and ODP Site 986, the higher resistivity may indicate the presence of hydrate in the shallow sediments between 4 and 10.5 km. High resistivities landward of the predicted GHSZ are also observed on both Line 1 (Fig. 10) and Line 2 (Fig. 11) which is consistent with the low velocity zones and bright amplitude reflectors seen in seismic data and may indicate the presence of shallow free gas accumulations (Sarkar *et al.* 2012). However, higher resistivities in the upper slope sediments may also result from reduction in porosity due to increased heterogeneity and glacial content in the area (Chabert *et al.* 2011; Sarkar *et al.* 2012).

Direct comparison of our resistivity models with other hydrate bearing areas of the world is difficult due to limited number of such studies and difference in the parameters affecting resistivity across the various hydrate provinces. If the porosity and background resistivity of the ODP Site 986 (Jansen *et al.* 1996) is assumed to be valid for the study area, the resistivities for the GHSZ can be compared to areas with similar porosity (50–60 per cent) and background resistivity (1–1.5 Ωm). The comparison can be limited further to resistivities in areas of hydrate presence derived from CSEM studies only for a like-to-like comparison. Resistivities of 3–12 Ωm in the Hikurangi Margin, offshore New Zealand (Schwalenberg *et al.* 2010a), around 4 Ωm in Porangahau Ridge, offshore New Zealand (Schwalenberg *et al.* 2010b), 3–5 Ωm in the Cascadia margin (Schwalenberg *et al.* 2005), and no greater than 5 Ωm for the Hydrate Ridge (Weitemeyer *et al.* 2006b, 2011) were reported, which are comparable to the values of resistivity reported here. These sites, however, were all in deeper water, with a more distal sediment supply without any glaciogenic component.

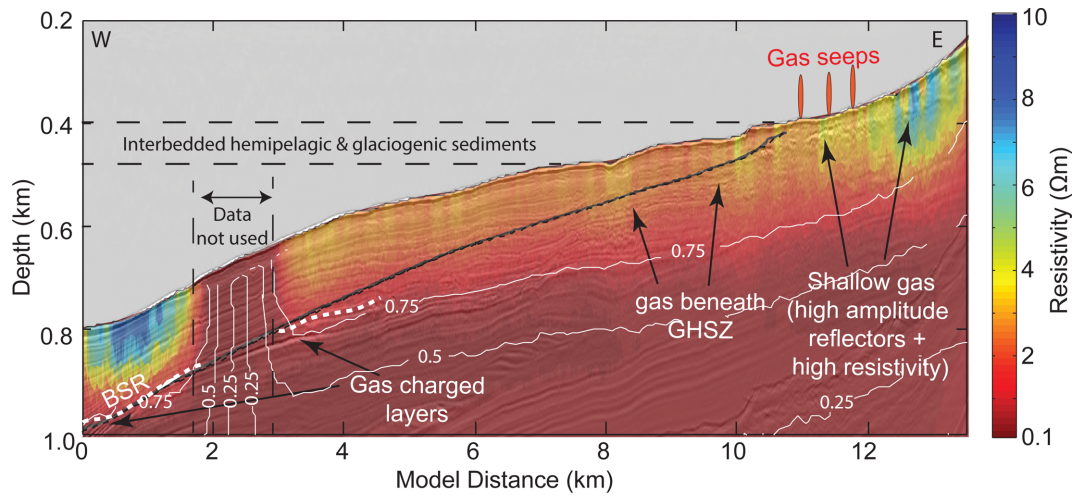


Figure 10. Overlay of vertical resistivity model from Vulcan inversion on coincident seismic reflection data for Line 1 (JR211-03 (Sarkar *et al.* 2012)) showing high resistivities above the BSR and bright amplitude reflectors associated with free gas. The dashed line marks the base of the GHSZ as per models of Marin-Moreno *et al.* (2013). Contour overlay (thin white line) shows data sensitivity to resistivity model (0.5 = 50 per cent sensitivity).

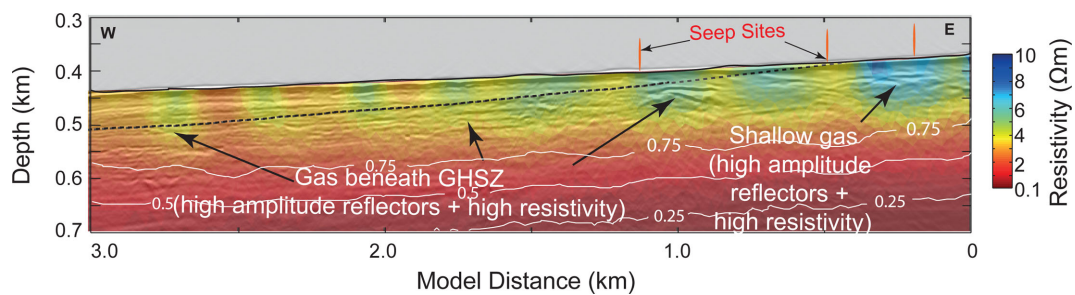


Figure 11. Overlay of vertical resistivity model from Vulcan inversion on coincident seismic reflection data for Line 2 (JR211-09 (Sarkar *et al.* 2012)) shows high resistivities within the shallow sediments. High amplitude reflectors associated with free gas are also observed on the seismic reflection data. The dashed line marks the base of the GHSZ from Marin-Moreno *et al.* (2013). Contour overlay (thin white line) shows data sensitivity to resistivity model (0.5 = 50 per cent sensitivity).

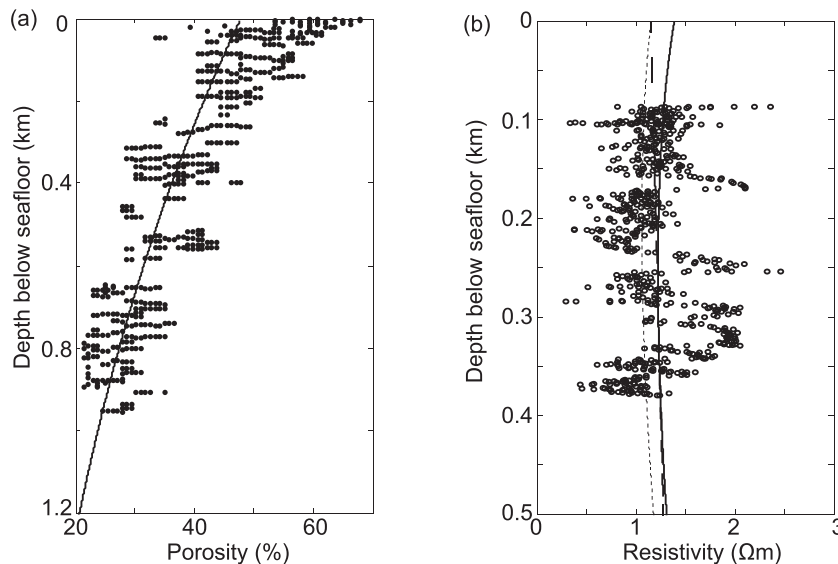


Figure 12. (a) A least-squares exponential fit (solid line) to the ODP porosity log (solid dots) (Jansen *et al.* 1996) is used for estimating saturation estimates for our study area. (b) Least-squares linear fit (dashed line) to the ODP resistivity log (circles) (Jansen *et al.* 1996) provide the background resistivity trend for water saturated sediments for our study area. Reasonable fits to this background trend can be obtained using Archie's equation (dotted line) for coefficients $m = n = 2$ and $a = 1$ and for the connectivity equation (solid line) of Lee (2011) using $\alpha = 3$ and $\mu = 2$.

Table 4. Shallow Hydrate and free gas saturations inferred for Line 1 and Line 2 using two different methods, Archie's Law (Archie 1942) (column 5) and a connectivity equation (Lee 2011) (column 6).

Line name	Depth interval	Model distance	Porosity	Archie (per cent)	Lee (per cent)	Constituent
Line 1	seabed–BSR	0–2 km	~45 per cent	25–60	20–55	Hydrate
Line 1	seabed–BSR	3.5–8 km	45–47 per cent	20–40	15–35	Hydrate
Line 1	seabed–BSR	8–10.5 km	47–49 per cent	20–50	15–45	Hydrate
Line 1	seabed–BSR	8–10.5 km	35 per cent	2–22	0–12	Hydrate
Line 1	seabed+ 200 m	10.5–13.5 km	~45 per cent	20–55	15–50	Free gas
Line 1	seabed+ 200 m	10.5–13.5 km	35 per cent	5–40	2–30	Free gas
Line 2	seabed+ 200 m	0–1 km	~45 per cent	25–55	20–50	Free gas
Line 2	seabed+ 200 m	0–1 km	35 per cent	10–35	8–30	Free gas
Line 2	seabed–BSR	1–3 km	46–47 per cent	10–35	4–25	Hydrate
Line 2	seabed–BSR	1–3 km	35 per cent	0–10	0–8	Hydrate

6.3.2 Estimating hydrate and free gas saturations

The resistivity models were used to infer pore space hydrate and free gas saturations in the study area. Considering the lack of direct information about many of the parameters affecting bulk resistivity in the area, quantitative interpretation of the resistivity models will contain large uncertainties. However, sensible values of porosity, pore fluid salinity and temperature may be obtained from previous geological, geophysical and oceanographic studies in the west Svalbard margin. Due to the similar influence of ocean currents on the depositional history of the continental basin and slope sediments (Eiken & Hinz 1993), ODP Site 986 is assumed to be fairly representative of the lithology of the slope sediments. Similarity in the porosity derived from seismic velocity at the Site S2 (water depth of 500 m) (Chabert *et al.* 2011), at the northern boundary of the study area and porosities observed at ODP Site 986 suggests the assumption of ODP Site 986 porosity is reasonable for the mid to deep slope. An exponential least-squared fit to the ODP porosity log (Fig. 12) was therefore used for the saturation estimates.

Since the presence of glacial sediments at the upper slope is likely to cause reduction in porosity (Chabert *et al.* 2011; Sarkar *et al.* 2012), gas and hydrate saturations for this area were also estimated using an average porosity of 35 per cent, similar to that used by Marín-Moreno *et al.* (2013) and Marín-Moreno *et al.* (2015a). Bottom water temperature variations in the area are available from the DASI CTD for 50 m above the seafloor. Pore-water resistivities were estimated using the bottom water temperatures and an average geothermal gradient of 55 °C km⁻¹ (Sarkar *et al.* 2012) using the relationship of Becker (1985). The commonly used Archie's equation (Archie 1942), was used to obtain hydrate and free gas saturations and can be expressed as:

$$S_w = \left[\frac{\rho_w a \phi^{-m}}{\rho} \right]^{\frac{1}{n}} \quad (1)$$

for pores partially filled with water and hydrate and/or gas. Here, S_w is the pore water saturation, ρ_w is the pore-water resistivity, ρ is the estimated resistivity, ϕ is the porosity and n is the saturation coefficient. The tortuosity constant, a , and cementation constant, m , are both related to the interconnection of pores in the sediment matrix. The degree of pore saturation of resistive material (hydrate and/or gas), S_R is then calculated from water saturation using:

$$S_R = 1 - S_w. \quad (2)$$

Commonly used values of $a = 1$ and $m = n = 2$ were found to fit the background resistivity trend derived from ODP Site 986. However, clay is abundant in the study area (Eiken & Hinz 1993; Forsberg *et al.* 1999), which requires a different equation to account for the additional clay conductivity effects (Mavko *et al.* 2009). Due to

lack of well logs to obtain required parameters, it was not feasible to use Waxman & Smits's (1968) equation to account for clay conductivity effect. A modified connectivity equation (Montaron 2009; Lee 2011), which provides an empirical approach to account for clay conductivity was used, to provide an alternative estimate of the hydrate and free gas saturations. The connectivity equation can be expressed as

$$\rho = \frac{a \rho_w}{(\phi S_w - \chi_w)^\mu}, \quad (3)$$

which can be rearranged to

$$S_w = \frac{1}{\phi} \left[\left(\frac{a \rho_w}{\rho} \right)^{\frac{1}{\mu}} + \chi_w \right]. \quad (4)$$

Here, χ_w is the water connectivity index (Montaron 2009). χ_w is expected to lie between $-0.2 \leq \chi_w \leq +0.2$ and can be approximated using the equation given by Lee (2011):

$$\chi_w = \alpha C_v \phi^\mu S_w, \quad (5)$$

where C_v is the clay percentage, μ is the conductivity coefficient, which ranges between 1.6 and 2, and α is an adjustable parameter determined from data with known ϕ and S_w (Lee 2011). In absence of direct constraints, $\mu = m = 2$, water saturated sediments ($S_w = 1$) and C_v values obtained from Forsberg *et al.* (1999) were used to calculate sediment resistivity using eqs (3) and (5) for different values α . A value of $\alpha = 3$ provided a good fit for the calculated sediment resistivity to the observed ODP Site 986 resistivity (Jansen *et al.* 1996; Fig. 12b). The calibrated value of α was then used to obtain the alternative hydrate and free gas saturation within the shallow sediments using eqs (2), (4) and (5).

Both Archie's equation and the connectivity equation assumed that hydrate and free gas replace pore waters and therefore provide saturation estimates as percentage of pore space which are shown in Table 4. In absence of velocity constraints, only hydrate presence is assumed as the cause of high resistivity within the predicted GHSZ. Free gas is assumed to be the cause of high resistivities outside the predicted GHSZ. However, hydrates can occupy veins and fractures in fine grained marine sediments (Lee & Collett 2009; Cook *et al.* 2010), which is not accounted for by the two methods. Nevertheless, the inferred hydrate saturations (Table 4) lie between the extremal bounds of saturation obtained using Hashin–Shtrikman (H–S) bounds of effective conductivity (Schmeling 1986) assuming 100 Ω for the resistivity of rock matrix. The H–S upper bound, which assumes conductive spherical inclusions within a resistive matrix, may better represent hydrates in fractures and veins (Weitemeyer *et al.* 2011). Use of this bound suggests 70–90 per cent hydrate saturation within the pore spaces of the GHSZ (35–48 per cent of

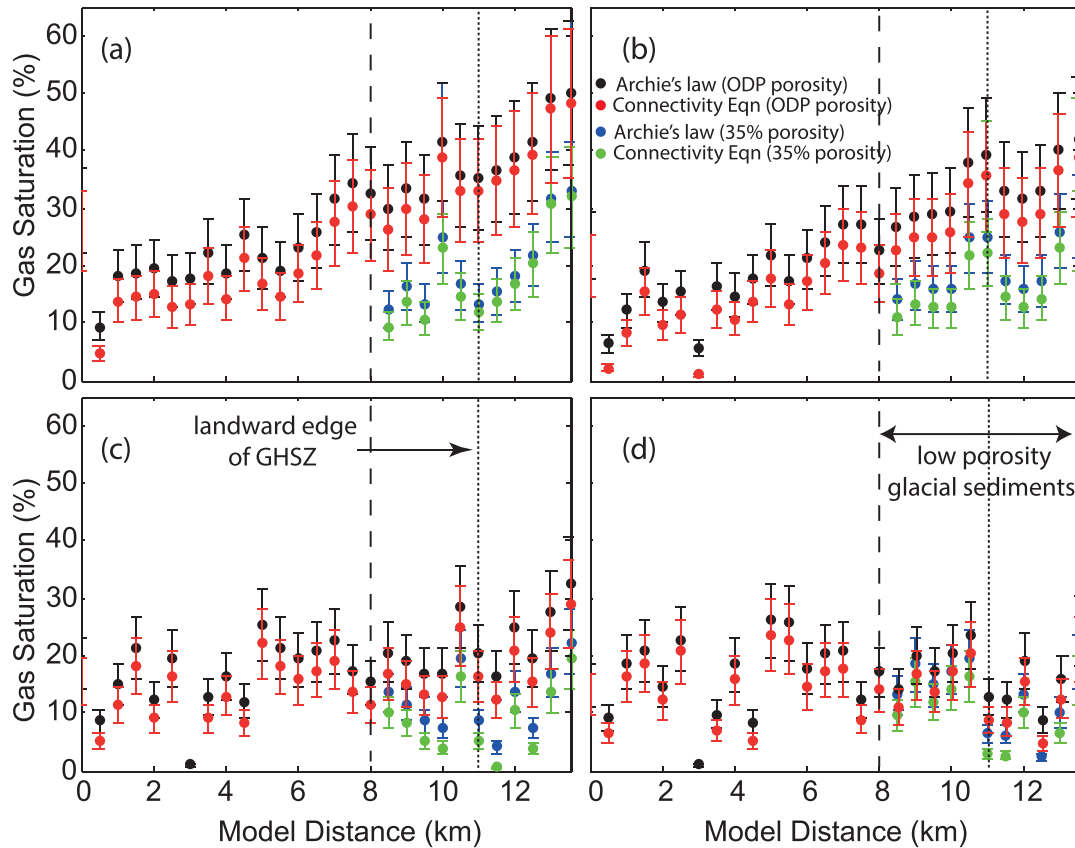


Figure 13. Depth averaged free gas saturation for incremental 100 m thick layers beneath the predicted base of gas hydrate stability zone. (a) 0–100 m beneath the GHSZ, (b) 100–200 m beneath GHSZ, (c) 200–300 m beneath GHSZ and (d) 300–400 m beneath the GHSZ. Between 10.5 (dotted vertical line) and 13.5 km model distance, the thickness of the GHSZ is 0 m. Depth averaged porosities from ODP Site 986 (Fig. 12a) are used to obtain saturation estimates for each depth interval (Black dots, Archie's law; Red dots, Connectivity equation (Lee 2011)). Between 8 and 13.5 km model distance, a constant 35 per cent porosity is assumed for alternative saturation estimates to account for low porosity glacial sediments (Blue dots, Archie's law; Green dots, Connectivity equation). Vertical dashed line at 8 km model distance marks the seaward extent of the lower porosity (35 per cent) glacial sediments.

bulk volume), whereas no hydrate saturation is obtained using the H–S lower bounds as the resistivities observed in our model are too low for this estimate.

Depth averaged free gas saturations were also inferred for incremental 100 m thick layers beneath the predicted base of GHSZ, using the OBE resistivity model for Line 1 (Fig. 13). A gradual increase in free gas saturation from 2–20 per cent at the lower slope sediments (0–2 km model distance, Fig. 13a) to 15–55 per cent at the edge of continental shelf (8–13 km model distance, Fig. 13a) was inferred for the first layer directly beneath the GHSZ. However, the maximum free gas saturation reduces to around 38 per cent when a lower porosity of 35 per cent was used for these estimates for the upper slope sediments (Fig. 13a). The average free gas saturations for the upper slope sediments was inferred to gradually decrease to the same level as the lower slope sediments in the subsequent layers (Fig. 13).

6.3.3 Interpretation of hydrate saturation estimates

The hydrate saturations inferred here are within the range of estimates suggested in other hydrate provinces such as the Cascadia margin (Schwalenberg *et al.* 2005) (up to 50 per cent), Hydrate Ridge (Weitemeyer *et al.* 2011) (up to 49 per cent) Porangahau Ridge (Schwalenberg *et al.* 2010a) (up to 17 per cent) and Hikurangi margin (26–68 per cent), where resistivity from CSEM data

were used for pore space saturation estimates using Archie's equation. The inferred hydrate saturations for the lower slope sediments, between 0 and 2 km model distance on Line 1 (Table 4) are, however, higher than previous estimates in the deep-water area based on seismic velocities (Westbrook *et al.* 2008; Hustoft *et al.* 2009; Chabert *et al.* 2011). These studies suggest a maximum hydrate saturation of 22 per cent (Chabert *et al.* 2011) and 2–25 per cent (Westbrook *et al.* 2008) at around 1300 m water depth. A 20 per cent reduction in the porosity of the top 100 mbsf (~45 per cent to 25 per cent) is required to better match the published deep water hydrate saturation estimates (~20 per cent), using the resistivities between 0 and 2 km on Line 1 and the connectivity equation (eq. 3). The inferred hydrate saturations for the mid and upper slope sediments (2–10.5 km model distance on Line 1; 1–3 km model distance on Line 2, Table 4) are also considerably higher than 2–5 per cent hydrate saturation for OBS sites N2 (866 m water depth) and S2 (480 m water depth) (Chabert *et al.* 2011) assuming the ODP Site 986 derived porosity trend. They are however comparable to the hydrate saturations estimated using 35 per cent average porosity between 8 and 10.5 km model distance on Line 1 and 1–3 km model distance on Line 2 (Table 4).

Modelling studies suggest that the GHSZ beneath 400–430 m water depth in the study area is vulnerable to increase in bottom water temperatures within the next century (Marín-Moreno *et al.* 2013, 2015a). Extrapolating the inferred average hydrate saturation for the seafloor depths of 400–430 m (15–45 per cent between 9

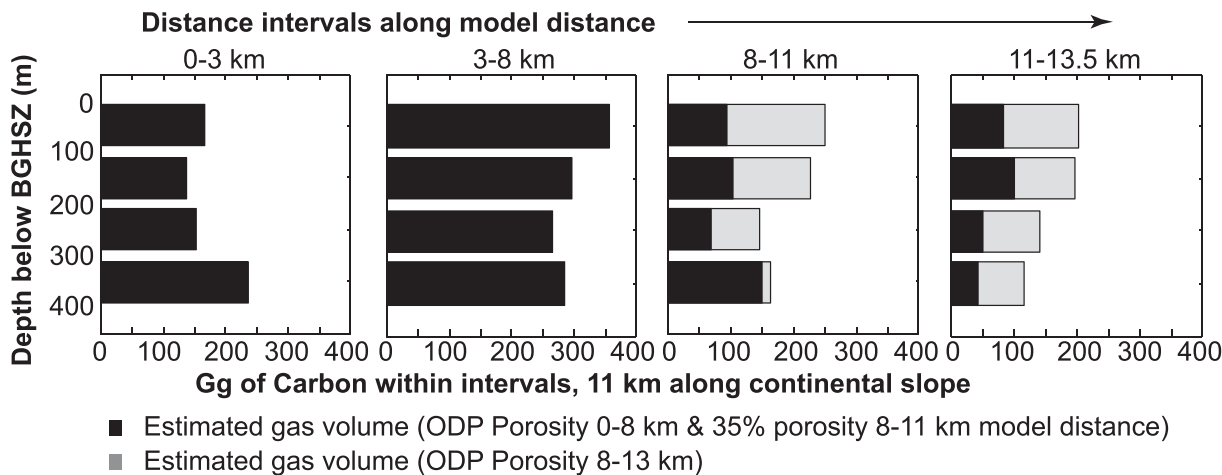


Figure 14. Estimated amounts of carbon present as methane within 100 m depth intervals beneath the base of GHSZ (as shown in Fig. 13) using average saturation values (from connectivity equation) derived from Fig. 13 for a 11 km long strip along the continental slope.

and 10.5 km model distance on Line 1, Table 4) to the 11 km long zone of active methane seeps in Area 3 reported by Sahling *et al.* (2014), 2530–7600 Gg of carbon (C) is inferred within this vulnerable hydrate reservoir. However, on assuming the reduced porosity of 35 per cent for the GHSZ within the upper slope and a maximum of 12 per cent hydrate saturation (Table 4), around 1310 Gg of carbon is inferred within this vulnerable zone. These estimates are presented assuming that the seafloor profile for Line 1 and Line 2 are representative for the entire Area 3 between 400 and 430 m water depth. The amount of carbon available for dissociation from hydrates in our estimates is an order of magnitude higher than the amount Marín-Moreno *et al.* (2015a) predicts may release in the next 100 yr. The model estimates of Marín-Moreno *et al.* (2015a) suggest only a part of the hydrate in the vulnerable zone will dissociate and some of the methane from dissociation will stay in the seabed as free gas.

6.3.4 Interpretation of free gas saturation estimates

The inferred free gas saturations at the landward edge of hydrate stability using both Archie and connectivity methods are very high. Such high saturations may overpressure the sediments located within the free gas zone and facilitate the flow of free gas towards the surface (Hornbach *et al.* 2004). A ~20 per cent further reduction in the ODP derived porosity (~45 per cent to 25 per cent) near the continental shelf edge would be required to obtain an average free gas saturation of 3–10 per cent as suggested by Chabert *et al.* (2011). Actual free gas saturations at the continental shelf edge are therefore likely to be lower than our estimates. However, high free gas saturations are likely to be present since the seeps on the upper slope and the continental shelf are still active (Westbrook *et al.* 2009; Berndt *et al.* 2014; Sahling *et al.* 2014) and are controlled by sub-surface lithological variations (Sarkar *et al.* 2012).

The vertical resistivity model from OBE inversion for Line 1 (Fig. 5) also shows high resistivities beneath the GHSZ, that are likely caused by the presence of free gas (Fig. 13). Previous estimates in the west Svalbard margin suggest 2–7 per cent of pore spaces saturated by free gas directly beneath the GHSZ and up to 9 per cent free gas saturation in lower slope sediments (Chabert *et al.* 2011). Average free gas saturations of around 8–50 per cent are inferred using Archie's equation and 2–48 per cent using the connectivity equation, beneath the GHSZ. The free gas zone be-

neath the GHSZ is also linked to the free gas zone at the edge of the continental shelf suggesting possible up-slope migration of free gas beneath the GHSZ Westbrook *et al.* (2009). A rough estimate using the inferred free gas saturations outside the GHSZ (Fig. 13) shows a large amount of carbon present in the form of free gas (Fig. 14). There is potentially more carbon in free gas form than within hydrates in the Area 3 (Sahling *et al.* 2014).

On the basis of seismic velocity structure (Ritzmann *et al.* 2004), the depth to the basement in our study area is estimated to be around 2–3 km beneath the seafloor at the eastern part of our profile with the sediment thickness increasing from east to west (Ritzmann *et al.* 2004). The deep resistivity feature in our model (6–17 Ωm) is therefore unlikely to be the basement as it is shallower than 2 km. In addition, basement rocks are likely to have resistivity greater than 100 Ωm . Synthetic model studies using the real survey parameters indicate that the resistive feature at the depth of the observed deep resistivity can be resolved by the data only in presence of a thick (>10 km) high resistivity (100 Ωm) beneath (Supporting Information Fig. S4). The deep resistive feature in our OBE model may therefore be caused by low porosity lithified sediments overlying the basement.

7 CONCLUSIONS

We analysed seafloor and towed receiver CSEM data along with high resolution seismic reflection data in a region of active methane seeps at the continental slope of west Svalbard margin. It has provided additional evidence and constraints for hydrate and free gas presence along the continental slope and at the continental shelf edge (Fig. 15). This study also provided a first look at the sub-surface resistivity structure of the continental slope area. The new resistivity information should help future studies to design more targeted electromagnetic studies in the area. Based on our analysis, we conclude that:

- (1) High resistivities (4–12 Ωm) within the predicted GHSZ and the presence of BSR in coincident seismic reflection data, suggest the presence of gas hydrate in the lower slope sediments. Average gas hydrate saturations of around 15–55 per cent are inferred here.
- (2) High resistivities (3–4 Ωm) within the predicted GHSZ of the upper slope sediments provide geophysical evidence for hydrate

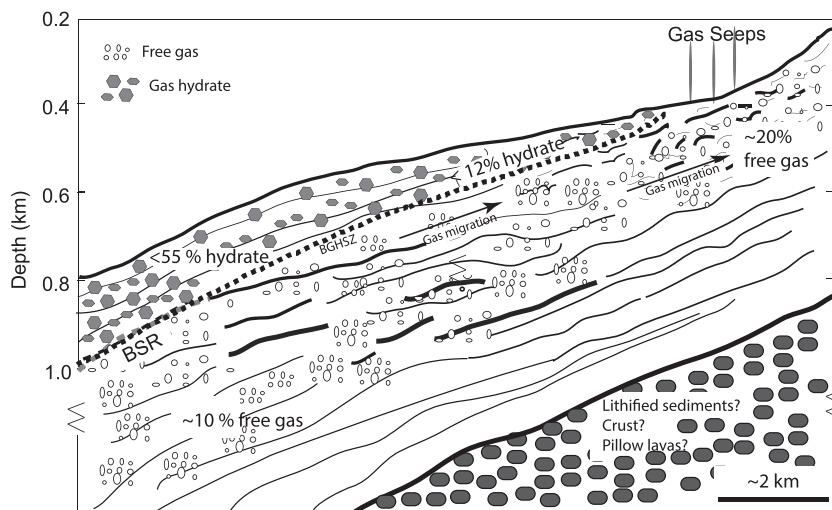


Figure 15. A sketch of the study area showing interpretations of hydrate and gas in the continental slope offshore Svalbard based on CSEM and seismic data. The vertical axis in the lower part of the figure is not to scale. Up to 12 per cent hydrate near the landward edge of the GHSZ and 15–55 per cent hydrate in the lower slope are inferred. Wide spread presence of free gas beneath the GHSZ is also inferred in the area.

presence in the area. Up to 12 per cent average hydrate saturation is inferred for the upper slope sediments.

(3) High resistivities around the landward edge of the GHSZ are consistent with low velocities and the presence of high amplitude reflectors in coincident seismic data (Sarkar *et al.* 2012) suggesting high free gas saturations. A free gas zone beneath the GHSZ with more than 10 per cent gas saturation is inferred to be linked to the zone of free gas escaping from the seabed near the continental shelf.

(4) There is thus a large volume of carbon in the form of free gas within the upper slope sediments.

ACKNOWLEDGEMENTS

We are grateful to the Captain, crew and shipboard scientific party of the RRS James Clark Ross cruise JCR269B for their hard work at sea. We are also thankful to Veit Huehnerbach for operating Hy-BIS, Laurence North and Yee Yuan Tan for their time during DASI operation and former PhD students, Amelia Astley, Anupama Rajan, Carolyn Graves, Helen Miller and Joan Campanya i Llovet for their hard work during the cruise. We would also like to thank Natural Environment Research Council's Ocean Bottom Instrumentation Facility and especially Ben Pitcairn and Robert Kirk for their onboard technical support. This research would not have been possible without the funding of the National Environment Research Council (NERC), UK (grant NE/H002732/1 and NE/H022260/1). TAM is supported by a Wolfson Research Merit award. Seismic and CSEM data are archived at the British Oceanographic Data Centre. We thank Kerry Key for developing the MARE2DEM code and making it publicly available and David Myer for the CSEM processing codes and valuable discussions. We thank reviewers Katrin Schwalenberg and Ann Cook for their suggestions to improve the manuscript.

REFERENCES

Archer, D., 2007. Methane hydrate stability and anthropogenic climate change, *Biogeosciences*, **4**(4), 521–544.
 Archie, G.E., 1942. The electrical resistivity log as an aid in determining some reservoir characteristics, *Trans. Am. Inst. Min. Eng.*, **146**, 54–62.

Attias, E., Weitemeyer, K.A., Minshull, T.A., Best, A., Sinha, M.C., Jeggen-Kulcsar, M., Holz, S. & Berndt, C., 2016. Controlled-source electromagnetic and seismic delineation of sub-seafloor fluid flow structures in a gas hydrate province, offshore Norway, *Geophys. J. Int.*, **206**, 1093–1110.
 Becker, K., 1985. Large scale electrical resistivity and bulk porosity of the oceanic crust, deep sea drilling project hole 504B, Tech. Rep., Initial Report, Deep Sea Drilling Project.
 Behrens, J.P., 2005. The detection of electrical anisotropy in 35 Ma pacific lithosphere: results from a marine controlled-source electromagnetic survey and implications for hydration of the upper mantle, *PhD thesis*, University of California, San Diego.
 Berndt, C. *et al.*, 2014. Temporal constraints on hydrate-controlled methane seepage off Svalbard, *Science*, **343**, 284–287.
 Biastoch, A. *et al.*, 2011. Rising Arctic Ocean temperatures cause gas hydrate destabilization and ocean acidification, *Geophys. Res. Lett.*, **38**(8), doi:10.1029/2011GL047222.
 Buland, A. & Kolbjørnsen, O., 2012. Bayesian inversion of CSEM and magnetotelluric data, *Geophysics*, **77**(1), E33–E42.
 Chabert, A., Minshull, T.A., Westbrook, G.K., Berndt, C., Thatcher, K.E. & Sarkar, S., 2011. Characterization of a stratigraphically constrained gas hydrate system along the western continental margin of Svalbard from ocean bottom seismometer data, *J. geophys. Res.*, **116**(B12), B12102, doi:10.1029/2011JB008211.
 Chen, J., Hoversten, G.M., Vasco, D., Rubin, Y. & Hou, Z., 2007. Special Section — Marine Controlled-Source Electromagnetic Methods: A Bayesian model for gas saturation estimation using marine seismic AVA and CSEM data, *Geophysics*, **72**(2), WA85–WA95.
 Collett, T.S. & Ladd, J., 2000. Detection of gas hydrate with downhole logs and assessment of gas hydrate concentrations (saturations) and gas volumes on the Blake Ridge with electrical resistivity log data, in *Proceedings of the Ocean Drilling Program, Scientific Results*, vol. 164, pp. 179–191, doi:10.2973/odp.proc.sr.164.219.2000.
 Constable, S., 2010. Ten years of marine CSEM for hydrocarbon exploration, *Geophysics*, **75**(5), 75A67–75A81.
 Constable, S.C., Parker, R.L. & Constable, G., 1987. Occam's Inversion: a practical algorithm for generating smooth models from electromagnetic sounding data, *Geophysics*, **52**(3), 289–300.
 Constable, S.C., Kannberg, P.K. & Weitemeyer, K.A., 2016. Vulcan: A deep-towed CSEM receiver, *Geochem. Geophys. Geosyst.*, **17**, 1042–1064.
 Cook, A.E., Anderson, B.I., Malinverno, A., Mrozewski, S. & Goldberg, D.S., 2010. Electrical anisotropy due to gas hydrate-filled fracture planes, *Geophysics*, **75**(6), F173–F185.

- Edwards, R.N., 1997. On the resource evaluation of marine gas hydrate deposits using sea-floor transient electric dipole-dipole methods, *Geophysics*, **62**(1), 63–74.
- Eiken, O. & Hinz, K., 1993. Contourites in the Fram Strait, *Sedimentary Geol.*, **82**(1–4), 15–32.
- Ellis, M.H., Sinha, M.C., Minshull, T.A., Sothcott, J. & Best, A.I., 2010. An anisotropic model for the electrical resistivity of two-phase geologic materials, *Geophysics*, **75**(6), E161–E170.
- Fisher, R.E. *et al.*, 2011. Arctic methane sources: Isotopic evidence for atmospheric inputs, *Geophys. Res. Lett.*, **38**, 3–8.
- Forsberg, C.F., Solheim, A., Jansen, E. & Andersen, E.S., 1999. The depositional environment of the western Svalbard margin during the late Pliocene and the Pleistocene: sedimentary facies at Site 986, in *Proceedings of the Ocean Drilling Program, Scientific Results*, vol. 162, pp. 233–246, doi:10.2973/odp.proc.sr.162.032.1999.
- Goswami, B.K., Weitemeyer, K.A., Minshull, T.A., Sinha, M.C., Westbrook, G.K., Chabert, A., Henstock, T.J. & Ker, S., 2015. A joint electromagnetic and seismic study of an active pockmark within the hydrate stability field at the Vestnesa Ridge, west Svalbard margin, *J. geophys. Res.*, **120**(10), 6797–6822.
- Hornbach, M.J., Saffer, D.M. & Holbrook, W.S., 2004. Critically pressured free-gas reservoirs below gas-hydrate provinces, *Nature*, **427**, 142–144.
- Hovland, M., Gardner, J.V. & Judd, A.G., 2002. The significance of pockmarks to understanding fluid flow processes and geohazards, *Geofluids*, **2**, 127–136.
- Hunter, S., Goldobin, D., Haywood, A.M., Ridgwell, A. & Rees, J., 2013. Sensitivity of the global submarine hydrate inventory to scenarios of future climate change, *Earth planet. Sci. Lett.*, **367**, 105–115.
- Hustoft, S., Bünz, S., Mienert, J. & Chand, S., 2009. Gas hydrate reservoir and active methane-venting province in sediments on <20 Ma young oceanic crust in the Fram Strait, offshore NW-Svalbard, *Earth planet. Sci. Lett.*, **284**(1–2), 12–24.
- Jakobsson, M., Macnab, R., Mayer, L., Anderson, R., Edwards, M., Hatzky, J., Schenke, H.W. & Johnson, P., 2008. An improved bathymetric portrayal of the Arctic Ocean: implications for ocean modeling and geological, geophysical and oceanographic analyses, *Geophys. Res. Lett.*, **35**(7), doi:10.1029/2008GL033520.
- Jansen, E., Raymo, M. & Blum, P., 1996. Shipboard Scientific Party 2 Hole 986A, in *Proceedings of the Ocean Drilling Program, Initial Reports*, vol. 162, pp. 287–342, Ocean Drilling Program, College Station, TX.
- Ker, S., Le Gonidec, Y., Marsset, B., Westbrook, G.K., Gibert, D. & Minshull, T.A., 2014. Fine-scale gas distribution in marine sediments assessed from deep-towed seismic data, *Geophys. J. Int.*, **196**(3), 1466–1470.
- Key, K., 2012. Marine EM inversion using unstructured grids: a 2D parallel adaptive finite element algorithm, in *SEG Las Vegas 2012 Annual Meeting*, **9**, 1–5.
- Key, K. & Lockwood, A., 2010. Determining the orientation of marine CSEM receivers using orthogonal Procrustes rotation analysis, *Geophysics*, **75**(3), F63–F70.
- Key, K. & Owall, J., 2011. A parallel goal-oriented adaptive finite element method for 2.5D electromagnetic modelling, *Geophys. J. Int.*, **186**(1), 137–154.
- Kretschmer, K., Biastoch, A., Rüpke, L. & Burwicz, E., 2015. Modeling the fate of methane hydrates under global warming, *Glob. Biogeochem. Cycles*, **29**, 610–625.
- Kvenvolden, K., 1993. Gas Hydrates- geological perspective and global change, *Rev. Geophys.*, **31**(2), 173–187.
- Lee, M.W., 2011. Connectivity Equation and Shaly-Sand Correction for Electrical Resistivity, Tech. Rep., USGS, 1–9.
- Lee, M.W. & Collett, T.S., 2009. Gas hydrate saturations estimated from fractured reservoir at Site NGHP-01-10, Krishna-Godavari Basin, India, *J. geophys. Res.*, **114**, B07102, doi:10.1029/2008JB006237.
- MacGregor, L. & Tomlinson, J., 2014. Special section : Interpretation and integration of CSEM data Marine controlled-source electromagnetic methods in the hydrocarbon industry: A tutorial on method and practice, *Interpretation*, **2**(3), 13–32.
- Marín-Moreno, H., Minshull, T.A., Westbrook, G.K., Sinha, B. & Sarkar, S., 2013. The response of methane hydrate beneath the seabed offshore Svalbard to ocean warming during the next three centuries, *Geophys. Res. Lett.*, **40**(19), 5159–5163.
- Marín-Moreno, H., Minshull, T., Westbrook, G.K. & Sinha, B., 2015a. Estimates of future warming-induced methane emissions from hydrate offshore west Svalbard for a range of climate models, *Geochem. Geophys. Geosyst.*, **16**, 1307–1323.
- Marín-Moreno, H., Giustiniani, M., Tinivella, U. & Piñero, E., 2015b. The challenges of quantifying the carbon stored in Arctic Marine gas hydrate, *Mar. Pet. Geol.*, **71**, 76–82.
- Mavko, G., Mukerji, T. & Dvorkin, J., 2009. *The Rock Physics Handbook*, pp. 1–511, Cambridge Univ. Press.
- Minshull, T., Sinha, M. & Pierce, C., 2005. Multi-disciplinary, sub-seabed geophysical imaging, *Sea Technol.*, **46**(10), 27–31.
- Montaron, B., 2009. Connectivity Theory—A New Approach To Modeling “Non-Archie” Rocks, *Petrophysics*, **50**(2), 102–115.
- Murton, B., Huhnerbach, V. & Garrard, J., 2012. Exploring ultradeep hydrothermal vents in the Cayman Trough by ROW, *Sea Technol.*, **53**(9), 15–20.
- Myer, D., Constable, S. & Key, K., 2011. Broad-band waveforms and robust processing for marine CSEM surveys, *Geophys. J. Int.*, **184**, 689–698.
- Myer, D., Key, K. & Constable, S., 2015. Marine CSEM of the Scarborough Gas Field, *Geophysics*, **80**(3), E187–E196.
- Panieri, G., Graves, C.A. & James, R.H., 2016. Paleo-methane emissions recorded in foraminifera near the landward limit of the gas hydrate stability zone offshore western Svalbard, *Geochem. Geophys. Geosyst.*, **17**, 521–537.
- Rajan, A., Mienert, J. & Bünz, S., 2012. Acoustic evidence for a gas migration and release system in Arctic glaciated continental margins offshore NW-Svalbard, *Mar. Pet. Geol.*, **32**, 36–49.
- Ramananjaona, C., MacGregor, L. & Andréis, D., 2011. Sensitivity and inversion of marine electromagnetic data in a vertically anisotropic stratified earth, *Geophys. Prospect.*, **59**(2), 341–360.
- Ray, A. & Key, K., 2012. Bayesian inversion of marine CSEM data with a trans-dimensional self parametrizing algorithm, *Geophys. J. Int.*, **191**, 1135–1151.
- Reagan, M.T. & Moridis, G.J., 2009. Large-scale simulation of methane hydrate dissociation along the West Spitsbergen Margin, *Geophys. Res. Lett.*, **36**(23), 1–5.
- Ritzmann, O., Jokat, W., Czuba, W., Guterch, A., Mjelde, R. & Nishimura, Y., 2004. A deep seismic transect from Hovgard Ridge to northwestern Svalbard across the continental-ocean transition: a sheared margin study, *Geophys. J. Int.*, **157**, 683–702.
- Sahling, H. *et al.*, 2014. Gas emissions at the continental margin west of Svalbard: mapping, sampling, and quantification, *Biogeosciences*, **11**(21), 6029–6046.
- Sarkar, S., Berndt, C., Chabert, A., Masson, D.G., Minshull, T.A. & Westbrook, G.K., 2011. Switching of a paleo-ice stream in northwest Svalbard, *Quat. Sci. Rev.*, **30**(13–14), 1710–1725.
- Sarkar, S., Berndt, C., Minshull, T.A., Westbrook, G.K., Klaeschen, D., Masson, D.G., Chabert, A. & Thatcher, K.E., 2012. Seismic evidence for shallow gas-escape features associated with a retreating gas hydrate zone offshore west Svalbard, *J. geophys. Res.*, **117**(B9), 1–18.
- Schmeling, H., 1986. Numerical models on the influence of partial melt on elastic and anelastic and electrical properties of rocks. Part II: Electrical conductivity, *Phys. Earth planet. Inter.*, **43**, 123–136.
- Schwalenberg, K., Willoughby, E., Mir, R. & Edwards, R.N., 2005. Marine gas hydrate electromagnetic signatures in Cascadia and their correlation with seismic blank zones, *First Break*, **23** (April), 57–63.
- Schwalenberg, K., Haeckel, M., Poort, J. & Jegen, M., 2010a. Evaluation of gas hydrate deposits in an active seep area using marine controlled source electromagnetics: results from Opouawe Bank, Hikurangi Margin, New Zealand, *Mar. Geol.*, **272**(1–4), 79–88.
- Schwalenberg, K., Wood, W., Pecher, I., Hamdan, L., Henrys, S., Jegen, M. & Coffin, R., 2010b. Preliminary interpretation of electromagnetic, heat flow, seismic, and geochemical data for gas hydrate distribution across the Porangahau Ridge, New Zealand, *Mar. Geol.*, **272**(1–4), 89–98.

- Sinha, M.C., Patel, P.D., Unsworth, M.J., Owen, T.R.E., McCormack, M.R.G. & Road, M., 1990. An Active Source Electromagnetic Sounding System for Marine Use, *Mar. Geophys. Res.*, **12**, 59–68.
- Smith, B.D. & Ward, S.H., 1974. On the Computation of Polarization Ellipse Parameters, *Geophysics*, **39**(6), 867–869.
- Solheim, A., Andersen, E., Elverhoi, A. & Fiedler, A., 1996. Late Cenozoic depositional history of the western Svalbard continental shelf, controlled by subsidence and climate, *Glob. Planet. Change*, **12**, 135–148.
- Thatcher, K.E., Westbrook, G.K., Sarkar, S. & Minshull, T.A., 2013. Methane release from warming-induced hydrate dissociation in the West Svalbard continental margin: Timing, rates, and geological controls, *J. geophys. Res.*, **118**, 1–17.
- Vogt, P.R., Crane, K., Sundvor, E., Max, M.D. & Pfirman, S.L., 1994. Methane-generated (?) pockmarks on young, thickly sedimented oceanic crust in the Arctic: Vestnesa ridge, Fram strait, *Geology*, **22**, 255–258.
- Waxman, M.H. & Smits, L.J.M., 1968. Electrical conductivities in oil-bearing shaly sands, *Soc. Pet. Eng. J.*, **8**, 107–122.
- Weitemeyer, K. & Constable, S., 2010. Mapping shallow geology and gas hydrate with marine CSEM surveys, *First Break*, **28** (June), 97–102.
- Weitemeyer, K., Constable, S. & Key, K., 2006a. Marine EM techniques for gas-hydrate detection and hazard mitigation, *Leading Edge*, **25**(5), 629–632.
- Weitemeyer, K.A., Constable, S.C., Key, K.W. & Behrens, J.P., 2006b. First results from a marine controlled-source electromagnetic survey to detect gas hydrates offshore Oregon, *Geophys. Res. Lett.*, **33**, L03304, doi:10.1029/2005GL024896.
- Weitemeyer, K.A., Constable, S. & Tréhu, A.M., 2011. A marine electromagnetic survey to detect gas hydrate at Hydrate Ridge, Oregon, *Geophys. J. Int.*, **187**(1), 45–62.
- Westbrook, G.K. *et al.*, 2008. Estimation of gas hydrate concentration from multi-component seismic data at sites on the continental margins of NW Svalbard and the Storegga region of Norway, *Mar. Pet. Geol.*, **25**(8), 744–758.
- Westbrook, G.K. *et al.*, 2009. Escape of methane gas from the seabed along the West Spitsbergen continental margin, *Geophys. Res. Lett.*, **36**(15), doi:10.1029/2009GL039191.

SUPPORTING INFORMATION

Additional Supporting Information may be found in the online version of this paper:

Figure S1. Isotropic resistivity models for Line 1 obtained from inversion of (a) Vulcan P-max data and (b) amplitude and phase OBE data shows high level of similarity to vertical resistivity models obtained from TIZ anisotropic inversion.

Figure S2. Isotropic resistivity model for Line 2 obtained from inversion of Vulcan P-max data shows high level of similarity to vertical resistivity models obtained from TIZ anisotropic inversion.

Figure S3. Vertical resistivity model (VTI anisotropic) for Line 7, shows high resistivities similar to that observed between 0–2 km model distance on Line 1.

Figure S4. (a) Synthetic model containing a 500 m thick 10 Ωm resistor 1.5 km beneath the seabed. This is followed by a 100 Ωm halfspace. (b) Inversion of synthetic data was able recover the 10 Ωm resistor in presence of the high resistivity half space beneath. (<http://gji.oxfordjournals.org/lookup/suppl/doi:10.1093/gji/ggw330/-/DC1>)

Please note: Oxford University Press is not responsible for the content or functionality of any supporting materials supplied by the authors. Any queries (other than missing material) should be directed to the corresponding author for the paper.